UC San Diego

UC San Diego Electronic Theses and Dissertations

Title

Investigation of Solar Energy Transfer through Plasmonic Au Nanoparticle-doped Sol-derived TiO$_2$ Thin Films in Photocatalysis and Photovoltaics /

Permalink

https://escholarship.org/uc/item/78x325f6

Author

Zelinski, Andrew

Publication Date

2013

Peer reviewed|Thesis/dissertation

UNIVERSITY OF CALIFORNIA, SAN DIEGO

Investigation of Solar Energy Transfer through Plasmonic Au Nanoparticle-doped Sol-derived TiO$_2$ Thin Films in Photocatalysis and Photovoltaics

A Thesis submitted in partial satisfaction of the requirements for the degree Master of Science

in

Engineering Sciences (Mechanical Engineering)

by

Andrew Zelinski

Committee in charge:

Professor Sungho Jin, Chair
Professor Prab Bandaru
Professor Donald Sirbuly
Professor Andrea Tao

2013

The Thesis of Andrew Zelinski is approved and it is acceptable in quality and form for the

publication on microfilm and electronically:

_____

_____

_____

_____

Chair

University of California, San Diego

2013

Table of Contents

List of Figures

List of Tables

ABSTRACT OF THE THESIS

Investigation of Solar Energy Transfer through Plasmonic Au Nanoparticle-doped Sol-derived

TiO$_2$ Thin Films in Photocatalysis and Photovoltaics

by

Andrew Zelinski

Master of Science in Engineering Sciences (Mechanical Engineering)

University of California, San Diego, 2013

Professor Sungho Jin, Chair

Titanium Dioxide (TiO$_2$) films were elaborated using the Sol-Gel technique and

subsequently used to study plasmonic photovoltaic and photocatalytic energy transfer

enhancement mechanisms. TiO$_2$ was chosen because of the unique optical and electrical

properties it possesses as well as its ease of preparation and operational stability. The properties

of sol-elaborated films vary significantly with processing environment and technique, and the sol

formula; a systematic investigation of these variables enabled the selection of a consistent

technique to produce relatively dense, crack-free TiO$_2$ thin films. Localized Surface Plasmon

Resonance (LSPR) energy transfer was investigated by integrating plasmonic Au nanoparticles

into multi-layer wide-band gap semiconductor (TiO$_2$) devices, and by doping strongly catalytic

TiO$_2$ anodes in a 3-electrode photochemical cell. An instant 3x photocurrent enhancement in the

multilayer solar cell device was observed under 650nm light illumination, which suggests the presence of a resonant energy transfer. The focus of this work was to develop a systematic analysis of the actual mechanics of energy transfer responsible for the light-harvesting enhancements seen in previous studies of Au nanoparticle-TiO_2 systems under visible illumination[15-29]. This mechanism remains the subject of debate and models have been proposed by various researchers. A method is developed here to pinpoint the most influential of the proposed mechanisms.

Introduction

Titanium Dioxide (TiO_2) has been the subject of extensive study in recent years owing to its promising optical, physical and dielectric properties as well as its chemical stability and potential for low-cost preparation. For example, it has been investigated for use in photovoltaics and as photocatalysts, gas sensors, Dye Sensitized Solar Cells, and optical coatings (1-4) Additionally, Titania's high refractive index (2.54 for anatase, 2.75 for rutile) and dielectric constant make it a suitable candidate for waveguiding applications.

For photovoltaic and photocatalyst applications, much research has been focused on improving the efficiency of devices by broadening the absorption bandwidth. Titania's wide band gap (3.2eV for anatase, 3.0eV for rutile) yields an absorption edge below 400nm, so only about 3-5% of total sunlight can activate the oxide to generate charge carriers that can ultimately be exploited to promote reduction and oxidation processes or provide potential to an external circuit. Thus, many efforts to modify Titania photocatalysts that can operate under UV and visible light are ongoing. TiO_2 is usually naturally n-doped due to the presence of oxygen vacancies; an appropriate adjacent electrolyte or metal creates a Schottky junction which can be exploited for the solar-to-fuel energy conversion or photovoltaic applications.

The material exists in three stable crystalline phases: brookite, rutile, and anatase. Titania thin films are traditionally prepared by sputtering or chemical vapour deposition (CVD), especially when studying photochemical or waveguiding functionality. These methods are limited by their high cost, high energy use, and small-scale of production. However, TiO_2 thin films can also be synthesized by the Sol-Gel method, an attractive alternative that benefits from good homogeneity and ease of composition control, low processing temperatures (~400C for anatase films, 1000C for rutile), considerably lower equipment cost, and high throughput. Sol-gel films

do tend to be porous and have lower refractive index than those produced by other methods, and sol- derived films can also present challenges in reproducibility and property consistency.[1-4] Thus, most studies on the use of TiO_2 for photovoltaic, photoelectrochemical and waveguiding applications have been based on films derived from CVD and Sputtering. The purpose of the first half this work is to present evidence that TiO_2 sol-gel films can be produced with sufficient consistency with respect to the advantageous optical and electrical properties of TiO_2 and consequently can supplant the expensive, labor intensive methods CVD and sputtering as the preferred fabrication technique for researchers studying applications involving solar-to-fuel and photovoltaic energy conversion through TiO_2 electrodes. The second half will employ the sol-derived films doped with Au nanoparticles to observe photo-enhancement in both electrochemical cells and solid state solar cells, by way of Localized Surface Plasmons, and will include an extensive investigation of the mechanism of photo-enhancement/energy conversion.

1 Sol-Derived TiO$_2$ Films

1.1 Sol-gel Science

Sol-gel films are produced by direct deposition of metal-Alkoxide-based solutions onto

substrates by spin or dip coating. Metal-Alkoxides have highly electronegative OR groups that

stabilize the metal in its highest oxidation state and render the metal susceptible to nucleophillic

attack, i.e. they are very reactive. Additional factors distinguish transition metal Alkoxides from

group-IV Alkoxides: lower electronegativity of transition metals causes them to be more

electrophillic and therefore are very unstable toward the hydrolysis and polycondensation

reactions and other nucleophillic reactions that proceed in the evolution of sol-gels. This greater

reactivity of transition metal Alkoxides necessitates stricter control of moisture and

environmental conditions.

Metal Alkoxide precursors in the presence of water undergo hydrolysis to form metal

hydroxides,

$$H_2O + M\text{-}OR \rightarrow HO\text{-}M \leftarrow O \begin{matrix} R \\ H \end{matrix} \rightarrow M\text{-}OH + ROH$$

,
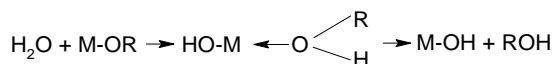
which then react with other metal Alkoxides in a process called alcoxolation (MOH + M-OR$\rightarrow$

MOM + ROH) or with other metal hydroxides in a process called oxolation

(MOH+MOH$\rightarrow$MOM + H$_2$0)[1]. The M-O-M bridges then begin to condense and, depending on

reaction kinetics, results in the gelation of the solution or the formation of precipitates which drop

out of the solution. Whether precipitation or gelation occurs depends on processing factors such

as pH gradients, temp, mixing rate as well as condensation kinetics. The amount of water added

to the sol is an important factor, as water reacts readily with the Alkoxides and is required to

ensure condensation into small particles or polymeric entities. Too much water, however, can cause the reaction kinetics to become uncontrollable. Even atmospheric moisture can make the condensation state of the sol uncontrolled and yield unpredictable results. Thus, environmental conditions must be controlled. Figure 3 gives a visual overview of the Sol-gel reaction process. A metal Alkoxide precursor is first diluted in an alcohol solvent. Water and an acid catalyst are introduced to begin the hydrolysis and condensation reactions and the evolution of the solution, or sol, into a gel. When sols are used to form thin films, total gelation is not desired and therefore the amount of water added must be carefully controlled: water is required to ensure the reactions proceed, but the amount added should be small enough to prevent the completion of the evolution of sol into a gel before depositing onto substrates for spin coating. The evolution from sol to gel is said to be complete when the solution does not flow upon tipping of its receptacle.

Acid catalysts can influence both the hydrolysis and the condensation rates and the structure of the condensed product. Acids protonate negatively charged Alkoxide groups, enhancing the hydrolysis reaction kinetics[1], and retard the condensation kinetics. Acid-catalyzed condensation is directed preferentially toward the ends rather than the middle chains resulting in more extended, less branched polymers (See Figure 3 for visual reference). Acid catalysts combined with low water/metal ratios in the Alkoxide promote evolution of monolithic gels.

The precursors can also be chemically modified, by substitution reactions at the metal bonds, to produce new molecular precursors. For example, Acetylacetone (Acac) can be employed as a chelating agent to prevent fast solution gelation and precipitation of oxide particles due to uncontrolled hydrolysis and condensation reactions after the addition of water.[1,3] When added to the metal Alkoxide precursor, the Acac bonds to the metal (substituting for a side group) which results in side group ligands of the precursor being preferentially hydrolyzed, and thus the

condensation kinetics and resulting structure are controlled. Even an excess amount of water does not hydrolyze all of the Acac ligands bonded to the metal.

The sol can be spin-coated onto a substrate and annealed to form a thin film. The material is totally amorphous just after deposition. Evaporation of the organic solvent and water molecules begins during the deposition process and continues through annealing. In the case of Titania sols, upon annealing at temperatures greater than 400C, an anatase crystal phase is nucleated and the alcohol is burned off, followed by sintering of the crystallites and (partial) elimination of residual porosity. The annealing step is critical for obtaining desired optical properties in the films since the microstructure depends largely on post-deposition treatments. Sol-derived Titania films are often porous, due to the rapid burn-off of organic residues and inadequate condensing and sintering, and with low density and hence, of lower refractive index. Electrical measurements on such films are prone to short-circuiting between measuring electrodes, therefore it is difficult to construct a practical device employing these films. However, density can be increased with careful control of the annealing process, including higher annealing temperatures and controlled temperature profiles, and with certain solvent selections that can be more readily burned off[1,8].

1.2   Experimental Part 1: TTIP Sol Films

Three different sol formulas involving a Titanium Tetra-Isopropoxide (TTIP) precursor were investigated and are summarized in the table below. In the first approach, TTIP: Isopropanol: HCl in a 1:26.5:1.5 molar ratio was formulated. A 0.7 N HCl mixture was prepared and added drop-wise to the TTIP:Isopropanol solvent mixture under rigorous stirring in open air. After 15 minutes of stirring, the sol was deposited onto glass (microscope slides) and p-type silicon substrates and spin-coated at 2500RPM for 20 seconds. The second method employed Ethanol (EtOH) as a solvent but otherwise was produced the same way. The constituents to the

second formula were TTIP:HCl:EtOH:HCl = 1:0.5:2:.05. In the third approach, HNO3 replaced

HCl as the acid catalyst and more solvent was used; TTIP:H20:HNO3:EtOH = 1:1:0.1:17. All

films were annealed at 500 ° C for 1 hr.

Table 1: Sol formulations based on Titanium (IV) Isopropoxide precursors

SOL Formula	Results
1. TTIP + HCL + Isopropanol +H20	Unstable
2. TTIP + HCl + EtOH + H20	Unstable
3. TTIP + HNO3 + EtOH + H20	Unstable

1.3   Results-TTIP Sol Films

The films produced from the sols described above were all of poor quality and

reproducibility. Despite numerous attempts to minimize the effects of the atmospheric conditions

and carefully ramp annealing temperatures to avoid thermal shock and cracking of the films, no

pure films were obtained. This is thought to be due to the extreme reactivity of the transition

metal Alkoxide to water. The ambient air moisture can react with the precursor and hydrolyze the

Titanium. At that point, the reaction kinetics are largely uncontrolled, and TiO_2 precipitates can

fall out of the sol before and during deposition. Images of films evolved in atmosphere with the

formulas listed above are shown in Figure 1. In (a) the inhomogeneity of a film produced with

formula 1 is seen as white precipitates throughout the film. In (b) the film can be seen as shattered

and flakey. Indeed, these films could simply be brushed off of the substrate with the swipe of a

finger, and thus were unusable.
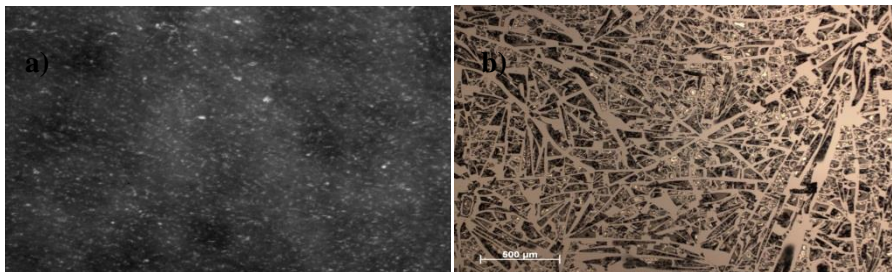
Figure 1: a) 100x magnified image of TiO2 film (formula #1) on glass substrate, calcined at 500C; b) Image of film deposited on p-type Si substrate calcined at 500C

For reference, sol residues from formula 3 were allowed to evolve into a gel under atmosphere and then were annealed at 500°C to form a powder. This powder was then characterized with X-ray Diffraction (Figure 2). The XRD peaks shown at 25°, 37°, and 48° correspond to the anatase peaks at (101), (004), and (200) crystal planes, respectively.[4]
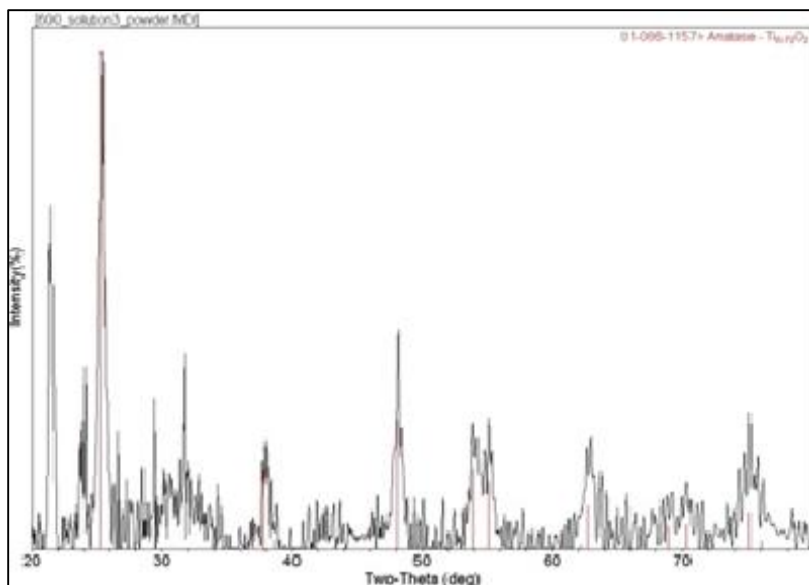
Figure 2: Powder diffraction results – sol formula 3. Characteristic anatase peaks are well-defined.

1.4   Discussion
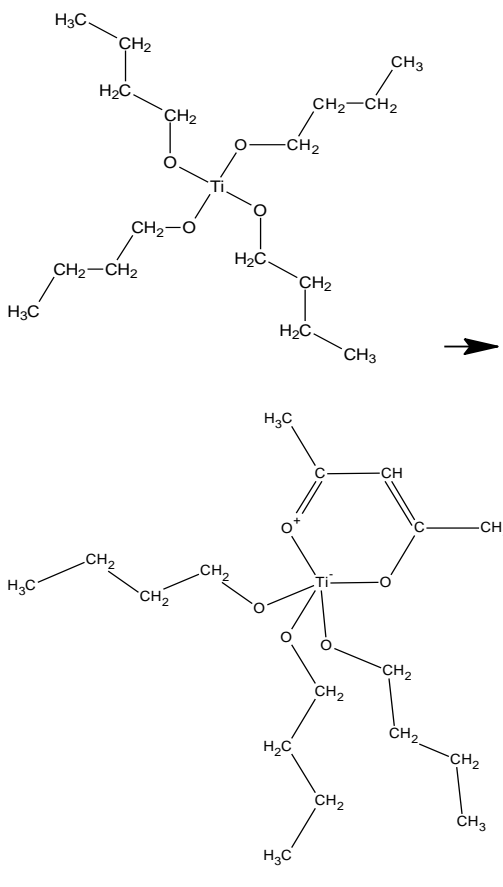
The XRD results presented in Figure 2 validate the sol formula in producing TiO_2 powder; the thin films produced with the same sols were unusable due to the uncontrolled nature

of the hydrolysis and polycondensation reactions in open air. As discussed above, film elaboration requires controlled reactions and the prevention of gelation and precipitation prior to deposition. Thus, a new sol formula was investigated that employed Acetylacetone (Acac) as a chelating agent to direct the crystallization morphology of the product. Tetrabutyl Orthotitanate ($Ti(OBu)_4$) was used as the precursor which was diluted in Butanol. The films produced with this method were of good quality and reproducibility and are described in detail below.
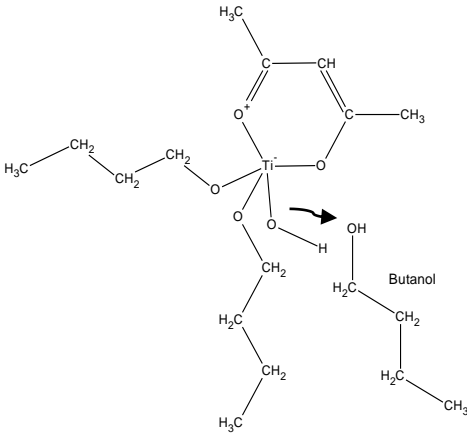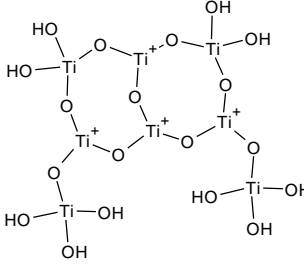
1.5   Experimental Part 2: $Ti(OBu)_4$ Sol Films

50ml of tert-Butanol was mixed with 59mmol of Acac under mixing. $Ti(OBu)_4$ (10g, 29mmol) was then added drop-wise to the solvent solution under rigorous stirring which continued for 15 minutes. In a separate container, H_2O (3.36g, 206mmol) was mixed with HNO_3 (.55g, 12mmol). This catalyst solution was then added drop-wise to the $Ti(OBu)_4$ solution and stirred for another 15 minutes. The resulting solution was tinted yellow due to the complexation of the Ti by the Acac, and was stable for weeks. The films were obtained by spin coating the sols onto plain or Indium-Tin-Oxide-coated glass microscope slides. Spinning is done at 2000 RPM for 40 sec. Annealing treatments were carried out in a Lindberg Blue M tube furnace with temperatures ranging from 350-600ºC. Figure 3 illustrates the hydrolysis and condensation process. Acetylacetone produces a chelated precursor as it increases the Ti coordination number from 4 to 5 while occupying two of its bonding sites. When water is added to the modified precursor, the butyl ligands are preferentially replaced by hydrolysis, thus the chelating agent controls and directs the structure of the condensed product. Oxolation between two hydroxyl ligands bonded to Ti, or Alkoxolation between a hydroxyl and a butyl both result in Ti-O-Ti bridge formation as the densification step proceeds. During moderate temperature annealing (400-500 C), organic residues from the solvent and Acetylacetone are slowly burned off, and the oxide network condenses into anatase structure. Not shown in the figure is the role of the Nitric Acid

catalyst, which protonate the Alkoxide groups and enhance the reaction kinetics by producing

good leaving groups[1].

TiO$_2$ Sol Production Step Description	Reaction Equation/ Structural Diagram
General Chemistry: Hydrolysis of metal- Alkoxide precursor	H_2O + M-OR ⟶ HO-M ⟵ O$\begin{smallmatrix}R\\H\end{smallmatrix}$ ⟶ M-OH + ROH
Chelation of Ti(OBu)$_4$	Ti(OBu)$_4$+ Acac ⟶ Ti(OBu)$_3$-Acac

Figure 3: Sol-Gel Evolution of Ti(OBu)$_4$ precursor. General chemistry of the hydrolysis is shown in the first row. The second row displays the chelation of the precursor by Acetylacetone.

TiO₂ Sol Production Step Description	Reaction Equation/ Structural Diagram
Hydrolysis of Chelated Ti(OBu)₄	$H_2O + Ti(OBu)_3\text{-acac} \rightarrow (HO)_3\text{-Ti-acac} + (OHBu)_3$
Condensation of hydrolyzed precursor via oxolation/Alkoxolation	$OH\text{-Ti-Acac} + OH\text{-Ti-Acac} \rightarrow Acac\text{-Ti-O-Ti-Acac} + H_2O$

Figure 4: Sol-Gel Evolution of Ti(OBu)₄ precursor, Continued. The chelation of the modified precursor is shown in row 3. The Acac occupies two bond sites of the metal while increasing its coordination number from 4 to 5. Water molecules hydrolyze the metal at a Butyl side group, which then obtains a proton from the attacking molecule and is removed as butanol – the common solvent. Oxolation/Alkoxolation condensation reactions then proceed (row 4).

1.5.1   Thickness Measurement

Thickness measurements were carried out using a Rudolph Auto EL ellipsometer. Since

the spin conditions were kept constant, it is assumed all film layers are approximately equal

before annealing. The measurements were obtained for films annealed at 400, 500, and 600° C.

1.5.2 X-ray Diffraction (XRD)

The crystalline morphology and microstructures of the resulting films was characterized with X-ray diffraction analysis. From the XRD data, crystallite size of the films can be deduced from line broadening using the Scherrer equation[11].

$$L = \frac{K\lambda}{\beta cos\theta}$$

Where L is the crystallite size of TiO2 thin films, K is a constant (0.94), λ is the wavelength of X-ray (CuKα= 1.5406 Å), β is the line broadening at half the maximum intensity in radians, and θ is the half diffraction angle of the centroid peak.

1.5.3 Porosity and Optical Properties

The refractive index of TiO_2 thin films was calculated from the measured absorbance spectrum using the analysis method of a weakly absorbing film deposited on a non-absorbing substrate[7]. In the case of weak absorption, transmission of a layer can be calculated from:

$$T = \frac{16n_0 n_1 n^2 \alpha}{C_1{}^2 + C_2{}^2 \alpha^2 + 2C_1 C_2 \alpha \cos\left(\frac{4\pi nt}{\lambda}\right)} \qquad (1)$$

where $C_1 = (n + n_0)/(n_1 + n)$, $C_2 = (n - n_0)/(n_1 - n)$, n_0 is the refractive index of air, n_1 is the refractive index of the substrate, $\alpha = e^{\frac{-4\pi kt}{\lambda}} = e^{-Kt}$ where K is the absorption coefficient of the thin film. In the weak and medium absorption regime, the dispersion of n and K is small. [5,7,14] The maximum and minimum of (1) occur for:

$$\frac{4\pi nt}{\lambda} = m\pi \qquad (2)$$

Where m is the order number. For TiO_2 on glass, ($n > n_1$, $C_2 < 0$), the extrema of (1):

$$T_{max} = 16 n_0 n_1 n^2 \alpha / (C_1 + C_2 \alpha)^2 \qquad (3)$$

$$T_{min} = 16 n_0 n_1 n^2 \alpha / (C_1 - C_2 \alpha)^2 \qquad (4)$$

Considering T_{max} and T_{min} as functions of λ through $n(\lambda)$ and $\alpha(\lambda)$, equations (3) and (4) are envelopes of the transmission spectrum. Taking the ratio of the two,

$$\alpha = \frac{C_1 [1 - (T_{max}/T_{min})^{1/2}]}{C_2 [1 + (T_{max}/T_{min})^{1/2}]}$$

Then from (3), the refractive index n can be determined from T_{max}, T_{min}, n_1, and n_0 at the same wavelength.

$$n = [N + (N^2 - n_0^2 n_1^2)^{1/2}]^{1/2} \qquad (5)$$

where $N = \frac{n_0^2 + n_1^2}{2} + 2 n_0 n_1 \frac{T_{max} - T_{min}}{T_{max} T_{min}}$.

Here, a simple linear extrapolation was performed around two adjacent minima of the absorption spectrum (Figure 6) to estimate the value of T_{min} at λ_{Tmax}. Values of T were calculated from the measured values of absorbance, A, from the relation

$$A = -\log(T\%/100).$$

The porosity of the thin films is calculated using[11]

$$Porosity = \left(1 - \frac{n^2 - 1}{n_d^2 - 1}\right) x \ 100\%$$

1.5.4 Electrical

Current-Voltage measurements were performed using an Agilent B1500 semiconductor analyzer in a 2-point probe configuration. For TiO_2 films on glass substrates, the probes were

spaced 1cm and oriented to investigate cross-plane resistivity of a single layered film at room temperature. A silver paste was used as contact pads for the Tungsten probes of the instrument. Silver paste has high surface roughness, so the work function is expected to be much less than the typical value for silver, 4.52eV. Thus, ohmic contact expected with TiO_2, which has an electron affinity of around 4.0 eV.[8] Both IV sweep and steady state IV-t measurements were performed. Through-plane measurements were performed as part of the studies on plasmonic energy transfer in the next section.

1.6   Results- Ti(OBu)₄ Sol Films

1.6.1   Effect of annealing process on crystalization, morphology

The film thickness decreased slightly as annealing temperature increased as shown in Table 2.

Table 2: Film thickness measured as a function of annealing temperature

Annealing Temperature, C	Thickness, nm
400	100
500	80
600	70

Figure 5 shows the XRD spectra for films annealed at 350, 400, and 500º C for 1 hr. The large background or scatter signal can be attributed to the glass substrates. As seen in the figure, TiO₂ crystallization onset occurs around 400 º C. Part b in figure shows the signal intensity results for a film calcined at 400 º. The small shoulder at 25 º corresponds to the (101) peak of anatase. The film in part c was calcined at 500º. The 101 peak is more pronounced, and the rest of the crystal planes seen in titania powders ((004) at 37 º and (200) at 48 º) begin to appear. The figure verifies that the film is amorphous at annealing temperatures less than 400º. From repeated analysis, we found crystalization of anatase phase to be thorough at temperatures starting at around 430º. The line broadening in part (c) was input into the Scherrer equation and a crystallite size of 17nm was calculated.
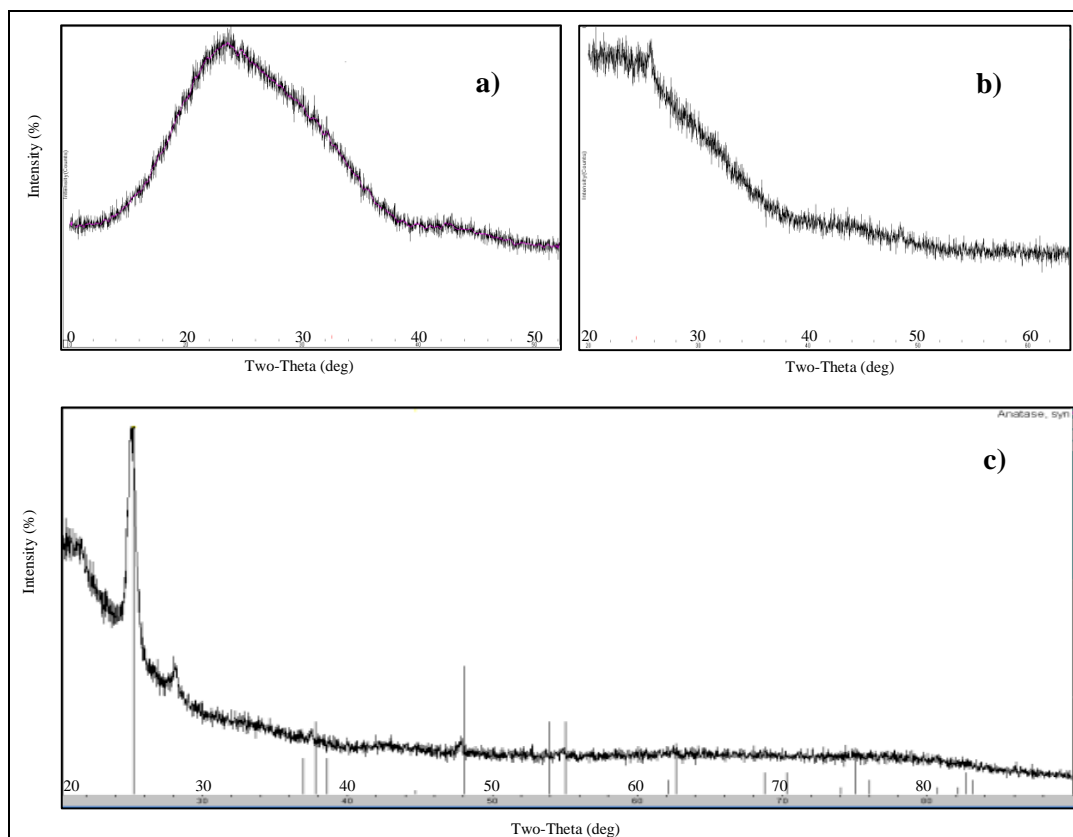
Figure 5: XRD results for Titania elaborated with Tetrabutyl Orthotitanate sols annealed at a) 350º b) 400 ° c) 500º for 1 hr.

Figure 5 shows the UV-Vis absorbance measurements of TiO_2 thin films on glass substrates

calcined at 350º, 500 °, and 600 ºC. For the film annealed at 500º, the temperature was carefully

ramped at ~ 0.2 degrees/second to the final temperature. The non-ramped annealing temperature

profile for the film annealed at 600 ° was ~ 2 degrees/ second. The total transmission decreases

as the annealing temperature increases, owing to the increase in density and thus an increase in

refractive index. For optical analysis, the films are assumed to be homogenous. The alternating

nature of the absorption spectra is due to interference effects between the Titania and the ITO.

The mismatch in the refractive indices of the two materials causes Fresnel loss to occur. The

curves enveloping the interference patterns are the T_{max} and T_{min} curves used to calculate

refractive index per the method described in (7).
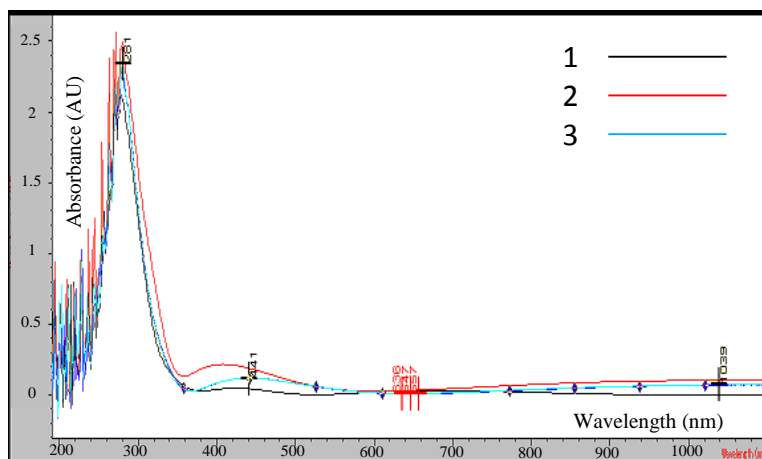
#	Name	Peaks (nm)	Abs (AU)	Valleys (nm)	Abs(AU)
1	300	278	2.1169	1060	3.78E-04
1		421	4.79E-02	1064	7.59E-04
1		656	3.11E-02	525	8.88E-04
2	600	281	2.49	603	2.55E-02
2		408	0.215	1051	1.03E-01
2		1048	0.104	1056	1.03E-01
3	500ramp	279	2.3	659	8.32E-03
3		441	0.117	368	2.80E-02
3		1047	7.05E-02	1044	6.96E-02

Figure 6: UV-Vis extinction spectra curve (a) and table (b) for films annealed at 300 (black), 500(blue), and 600 (red) degrees

The results of the refractive index and porosity estimations are listed in Table 3. As expected, refractive index increases and porosity decreases with increasing annealing temperature. The films elaborated with this approach initially tended to suffer from macroscopic cracking, as seen in the images in Figure 7. Fan *et. al* (8) attributed this cracking to the sintering process. Specifically, rapid heating causes the fast removal of unwanted solvent and catalyst residues from the material and which causes the film to be porous, and cracks can develop due to

the mismatch in the thermal expansion coefficients of the film and substrate. However, we found that total annealing temperature was far more influential on porosity than temperature ramping, and temporal temperature profiles during annealing seemingly had no impact on the development of cracks in the film. Porosity decreased with increasing annealing temperature, and the development of microscopic cracks seemed independent of annealing temperatures above 400.

Table 3: Refractive Index and Porosity calculation results for TiO2 films annealed at various temperatures

Annealing Temperature, C	Refractive Index, n	Porosity (%)
500 (slow temperature ramp)	2.08	37
600	2.26	23
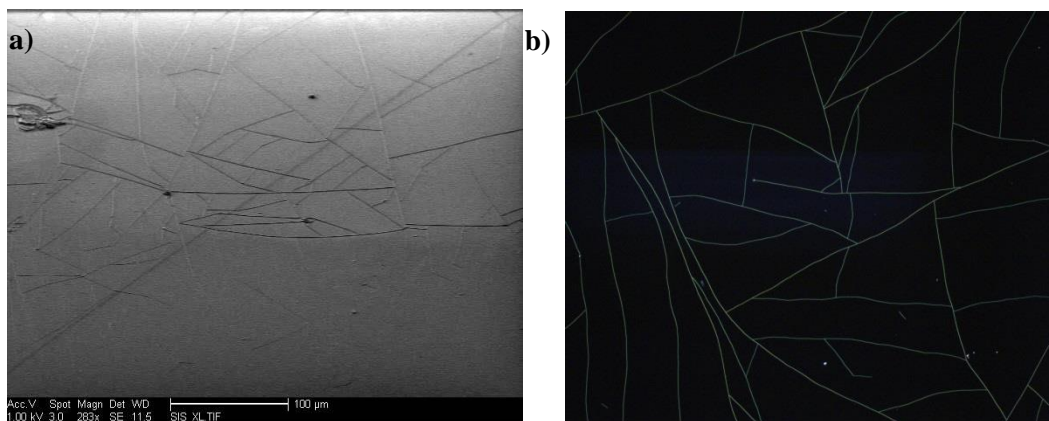
Figure 7: Scanning Electron (a) and Optical Microscope Dark Field (b) images of cracked Titania films.

However, it cannot be concluded that thermal expansion mismatch between TiO_2 thin films and the substrates did not play a role in the cracking. We propose that cooling profiles might have a larger effect than the heating profiles, as the cracking could be observed under a microscope when the films were removed from the furnace and placed on the cool metal microscope platform. Nevertheless, we found a surprising solution to the cracking problem that was

irrespective of temperature ramping. Preparing the sols at 1/50th of the prescribed batch size (i.e. 1 ml Butanol instead of 50ml, 0.2ml TiOBu$_4$, instead of 10ml, etc.) lead to reproducibly crack- free films. This is most likely ascribed to the limiting of exposure to atmospheric moisture and contaminants and thus maintaining stoichiometry of sols. Because the constituents are all mixed in a drop-wise fashion, a small batch is exposed to air for a much smaller time period, resulting in purer and higher quality sols. The images in Figure 8 are of crack-free films that were obtained from a small sol batch. All characterizations were performed on crack-free films.
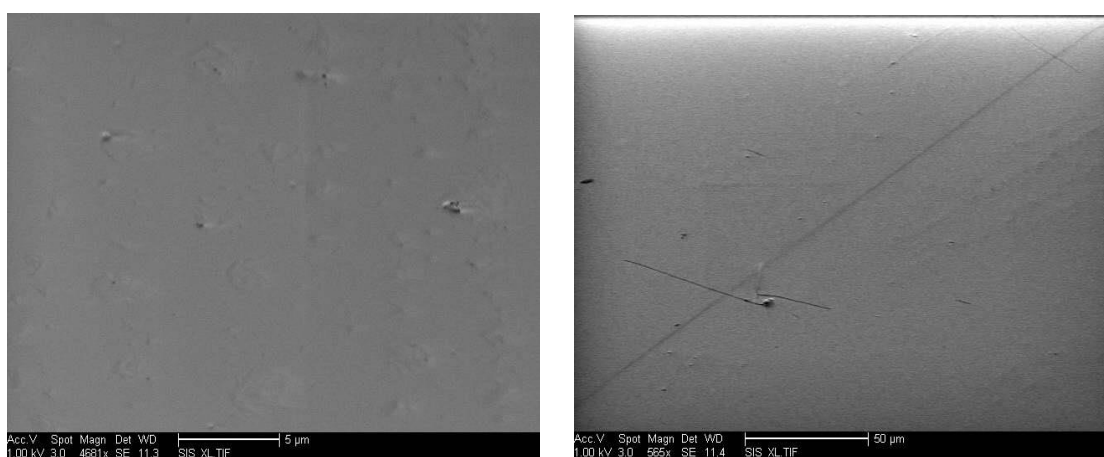
Figure 8: Scanning Electron Microscope images of crack-free Titania films

1.6.2 Electrical Properties

The films are highly resistive to cross-plane (parallel to surface) current, with resistance values on the order of 10^9-10^{10} Ω. Typical IV sweep and IV-t plots are shown in Figure 9. The symmetry of the curve in Figure 9(a) indicates the ohmic conduction over the measured voltage range. The noise of the curve is not well understood. Possible explanations include limitations of the internal electronics of the instrument when measuring nanoscale currents, the composite impedance taking into account TiO2-Ag and Ag-W contacts and internal circuitry as well as the dielectric properties of the environment, or the periodic emptying of trap states and relative inhomogeneity of polycrystalline films.
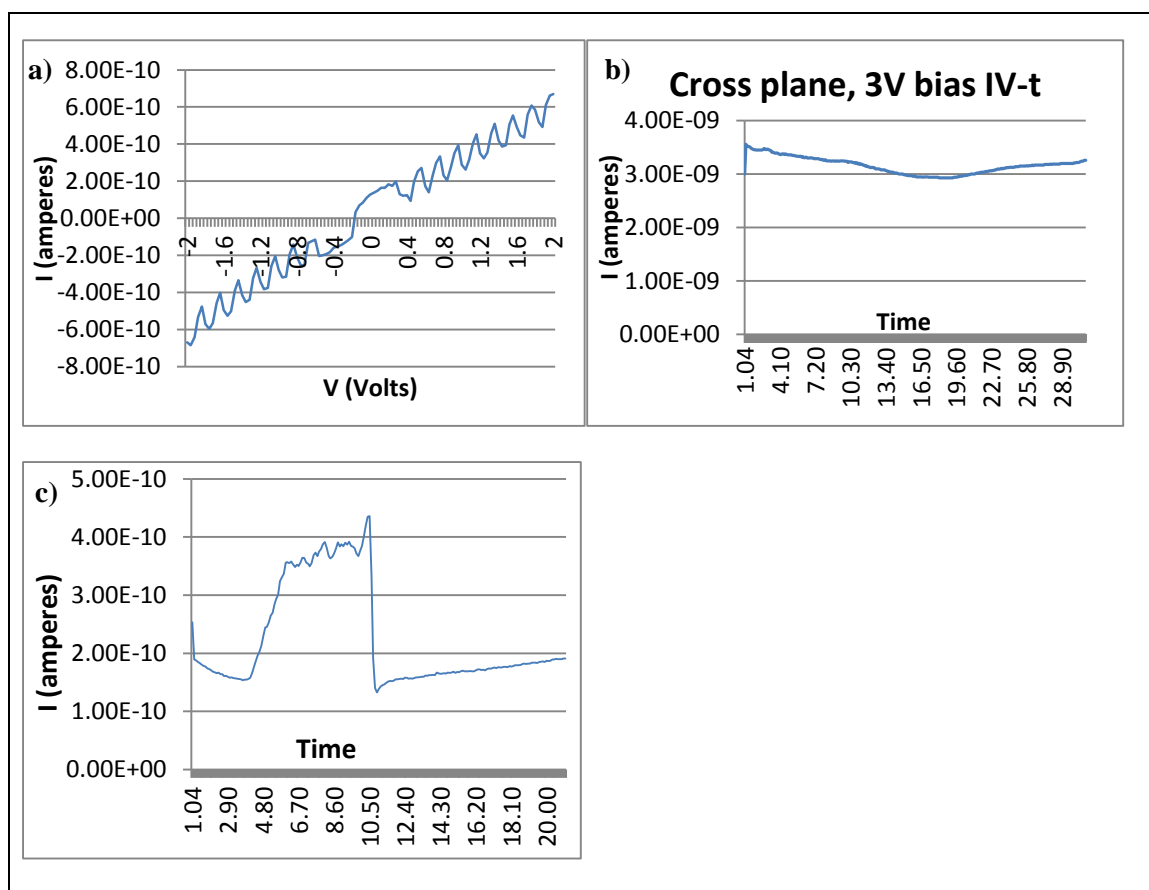
Figure 9: IV sweep (a) and IV-t (b) curves for single layer TiO_2 films on glass substrates. A 3V bias was applied to the sample for IV-t measurements. In part c, Short wave ultra violet light was irradiated, resulting in increased current due to increased carrier concentration.

The high resistance is expected and is also attributed to the polycrystalline nature of the films. Electronic conduction is dependent upon the extent of carrier trapping at grain boundaries of the film. Because polycrystalline semiconductors contain defects caused by incomplete bonding between adjacent crystallites, disordered material in the boundary region results in trapping states, space charge regions, and local potential barriers. The conductivity σ is given by:

$$\sigma = q\mu(T)n(T).$$

The carrier mobility $\mu(T)$ depends on the intergrain potential barrier V_B:

$$\mu(T) \propto \exp\left[-\frac{qV_B}{kT}\right]$$

and the carrier concentration $n(T)$ depends on the trap depth of surface states (E_c-E_t) and V_B:

$$n(T) \propto \exp\left[-\frac{E_C - E_t - qV_B}{kT}\right]$$

Carriers arise from the extent of intrinsic n-doping of the film from oxygen vacancies. Non-uniformity in grain size and fluctuations in dopant concentrations between grains contribute to a variety of grain potentials distributed between large non-depleted grains and fine totally depleted grains, resulting in different E_C-E_F from grain to grain. It is reasonable to assume that over the length of 1cm, there will be regions of very low carrier concentration (when trap depth is large) as well as low carrier mobility (when intergrain potential is large). Thus, very high resistance values were obtained for the in-plane measurements.

2 Solar Energy Conversion Through Plasmonics

2.1 Surface Plasmons

Photovoltaics, the conversion of solar energy into electric energy, and Photocatalytics, the efficient production of chemical fuels using sunlight energy, are of the most attractive, sustainable solutions to global energy problem. For example, hydrogen production via photoelectrochemical water splitting is a single-step process that chemically stores sunlight energy. Effectiveness of solar-driven photovolataic and photocatalytic processes depends upon the ability of the semiconductors to absorb as much as the solar spectrum as possible, and then suppress recombination of photogenerated charge carriers which drive photochemical reactions in electrochemical cells or contribute to current in photovoltaic cells . Currently, no material combination and device configuration has been able to achieve high enough efficiency in energy conversion to meet low-cost requirements or become a stable, feasible candidate for large-scale production. Because oxide semiconductors such as TiO_2 can be made with low cost methods and are usually stable in aqueous environments, they make good candidates for further investigation. Intrinsically, TiO_2 is a weak absorber of visible and infrared light, and thus would not alone be sufficient for solar applications. Metal nanoparticles have been shown to increase solar absorption in a TiO_2 electrode by absorbing visible light by way of localized surface plasmon oscillations[17-23] and are of great interest because of their electronic, optical and magnetic properties. Gold nanoparticles have a surface plasmon resonance in the visible portion of the electromagnetic spectrum that is dependent of the size and shape of the nanoparticle, the distance between particles, and the dielectric property of the surrounding medium. Thus, their electronic and optical properties can be finely tuned.

Plasmon absorbance of gold nanoparticles has been exploited for sensing applications and has been demonstrated as a feasible choice for plasmon-induced photochemical reactions. If a plasmon-excited metal nanoparticle can efficiently harvest light and transfer energy to a semiconducting medium without degradation, a new generation of photocatalysts and photovoltaics can be realized.

As stated above, one of the most interesting photochemical reactions that could benefit from plasmonic energy transfer is water-splitting. The photocatalytic splitting of water into Hydrogen and Oxygen presents a promising alternative for tapping the energy of the Sun; the chemical storage of solar energy in Hydrogen has been the subject of research for many years. Typical photoelectrodes lack the ability to harness the visible and infrared portion of the solar spectrum. This technology would benefit greatly from plasmonic absorption of visible light and the subsequent energy transfer into surrounding semiconductor medium

Surface plasmons are collective oscillations of electrons driven by impinging electromagnetic fields. The excitation of localized surface plasmons is a resonant process with a resonance frequency that is determined by composition, size, and shape of the metal nanoparticle and its dielectric environment. At resonant frequencies, these charge oscillations produce intense local electromagnetic fields near the metal and causes strong light scattering. In metal nanoparticles smaller than the wavelength of light, all atoms in the particle can be excited. The collective oscillation then can be interpreted as a displacement of the center of mass of all electrons in the particle against the positively charged background of the atomic cores, and is usually modeled using the Mie Scattering theory (figure 10).
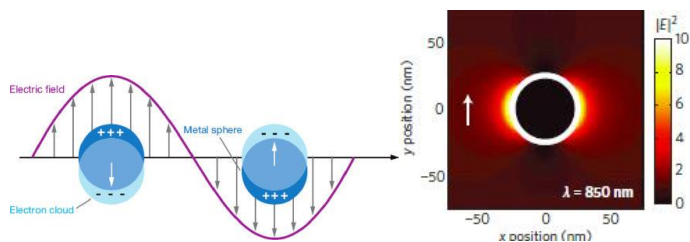
Figure 10: a) Resultant electron oscillation in the presence of impinging electromagnetic field; b) electromagnetic simulation of field intensity. Hot-spot regions shown in yellow

Plasmonic modes are largely analogous to molecular orbitals. The modes of adjacent nanoparticles can hybridize and yield a high energy, subradiant "anti-bonding" mode and a lower energy, super-radiant "bonding" mode. These differ in their coupling to incident light: in the low-energy mode, mutually aligned dipoles result in large induced dipoles and strong coupling to far field. These are "bright plasmons." The high-energy mode, with anti-aligned dipoles (no net dipole) are referred to as "dark modes" and do not couple to far field. In the bright or super-radiant mode, the plasmon induced electromagnetic fields interact constructively to result in local "hot spot" regions at which the field intensity reaches 1000 times that of the incident electric field intensity. Particles that support surface plasmons are colloquially referred to as optical antennas, as this charge oscillation-electromagnetic field interaction is an optical analogy of the function of radio antennas. The intense light trapping and focusing properties have been researched for a wide array of applications including sensing, non-linear optics, plasmonic IC's, and energy conversion devices.

Plasmon-induced photochemical reactions and photocurrent enhancement of semiconductor cells has been demonstrated[17-23]. In some cases, photocurrent/photopotential and photoelectrochemical action spectra responses coincided very well with the absorption spectra of the nanoparticles in the film, providing prima facie evidence that the plasmonic absorption of

irradiation was directly responsible for the observed increases in photocurrents and photopotentials. However, specific mechanisms of energy transfer in the photo responses are not well understood. For the case of Au nanoparticles embedded in Fe_2O_3 , with a bandgap of 2.1 eV, increases in photocurrent in a photochemical cell might be explained simply by the exciton-plasmon interactions and increased efficiency of absorption in the semiconductor by the near field enhancement by the nanoparticle: the absorption length of the semiconductor (0.1-1μm) is much longer than the carrier diffusion length, so many photogenerated electron-hole pairs cannot reach the surface and participate in photochemical reactions. Metal nanoparticle surface plasmons concentrate incident electromagnetic energy near the surface to be harvested by the absorber. However, for large band-gap materials like TiO_2, this explanation is not sufficient, since TiO_2 does not intrinsically absorb in the plasmon frequency range. It is worth-while to review the mechanisms proposed by various researchers. In all cases, the researchers first found an increase in photocurrent of a 3-electrode photochemical cell setup to coincide with the absorption spectrum of the nanoparticles, which verifies the plasmon is likely responsible for the enhancements.

2.2   Plasmonic Energy Transfer Models

The three predominant explanations of plasmonic light-matter interactions responsible for observed photoaction enhancements are titled in the figure below.

H. Atwater. *Nature Materials*. 2010, 9, 205-213
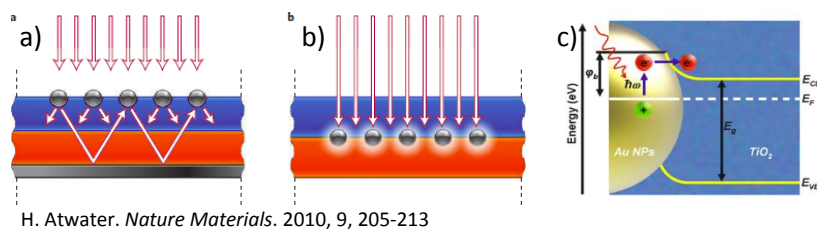
Figure 11: a) Light Scattering, b) Light Concentration, c) Hot e-h pair Generation

2.2.1   Charge Separation – Sensitization Model

Early attempts to characterize the resonant energy transfer to a semiconducting medium involved a basic charge separation model. This model, proposed by Tian *et. al*, is based on the transfer of a plasmon-excited electron from the gold nanoparticle to the TiO_2 conduction band. An electron-hole pair in the nanoparticle is created by the plasmon resonance, and contains enough energy to traverse the Schottky barrier formed at the Au-TiO_2 interface. The electron is transferred to the TiO_2 while the hole is filled by an appropriate donor in solution. A schematic of this model is presented in Figure 12 [22].
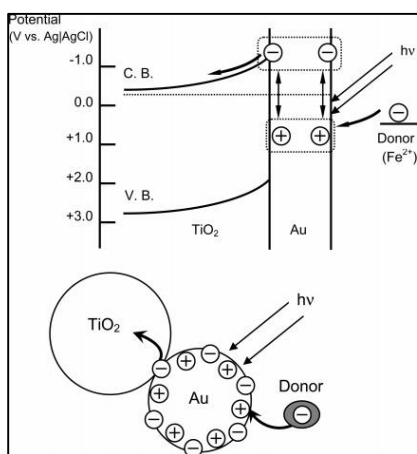
Figure 12: Charge separation model is analogous to the operation of a Dye-Sensitized solar cell.

The evidence presented for this model was the photocatalytic oxidation of ethanol and methanol from TiO_2- Au films, and a purported transient increase in absorption at a single wavelength of a TiO_2-Au film in the presence of a donor, and an immediate drop in both with addition of an electron acceptor, O_2, leading them to believe charge was directly transferred. But this evidence does not preclude the other two mechanisms, described below, and is thus not a

complete model. Additionally, although they describe the charge separation of plasmon-excited particles, their model does not completely prescribe the requirement of a plasmon resonance to observe current enhancements; metal charging effects and Fermi-level equilibration results in a system by which electron-hole pairs can be excited with any light with enough energy to promote the electrons over the Schottky barrier. The model also does not explain the absence of electron screening effects, which would be large in metal particles with large concentrations of electrons.

2.2.2   Light Scattering Model

The increased absorption and photoaction in the spectra for metal nanoparticle-semiconductor films might be explained simply by an enhancement of the optical path lengths of scattered light.[28] Nanoparticles close to an interface between two dielectrics preferentially scatter light into the dielectric with larger permittivity. The scattered light then acquires and angular spread that increases its optical path length; light scattered beyond a critical angle will be trapped in the cell. If the cell has a reflecting back contact, the light will be re-radiated by the same scattering particles as it takes several passes through cell. Size and shape of the particles are the key factors of this property. Smaller particles with dipole moment closer to the semiconductor layer will couple more incident light because of enhanced near-field coupling and thus better forward anisotropy. Smaller particles however suffer more ohmic losses and have a decreased scattering rate. The distance from the substrate of the particles also influences the observed enhancements: spacing them further from the substrate helps avoid destructive interference at a cost of reduced near-field coupling. Thus, the optimization of photoresponse according to this model involves a delicate balancing of these factors.

2.2.3 Light Concentration Model

Liu *et. al* [21] proposed shortcomings to the charge transfer model. Namely, surface plasmons are not similar to electron-hole pairs because there is no highest occupied molecular orbital-lowest unoccupied molecular orbital (HOMO-LUMO) energy separation. The Liu group developed a model for the photocatalytic enhancement mechanism based solely on the near-field optical enhancement of the Au nanoparticles, and reasoned that the enhanced photocatalytic water splitting under visible illumination in TiO_2 film could be explained without charge transfers. Both absorption spectra and photocatalytic enhancement were investigated with an N and F defect-rich TiO_2 prepared by anodization of Titanium foils as well as a defect-free TiO_2 film prepared by the sol-gel method. The sol-gel film showed no absorption in the visible region, and with Au nanoparticles deposited on top, did not enhance photocatalytic activity. In contrast, the impurity doped TiO_2 showed significant absorption in the visible range and significant photocurrent enhancement in the photochemical cell. Thus, a model was proposed[21] based solely on the presence of impurities in the TiO_2 film (Figure 13). Impurities create defect states in the bandgap. If the impurity is within carrier diffusion length of the surface, an excited carrier from mid-gap states can contribute to catalytic processes. The strong near-field optical enhancement produced by plasmonic nanoparticles creates strong electromagnetic fields near the surface which excite these impurities. The nanoparticles therefore serve as antennas to concentrate the electromagnetic fields to promote carriers from defect states.
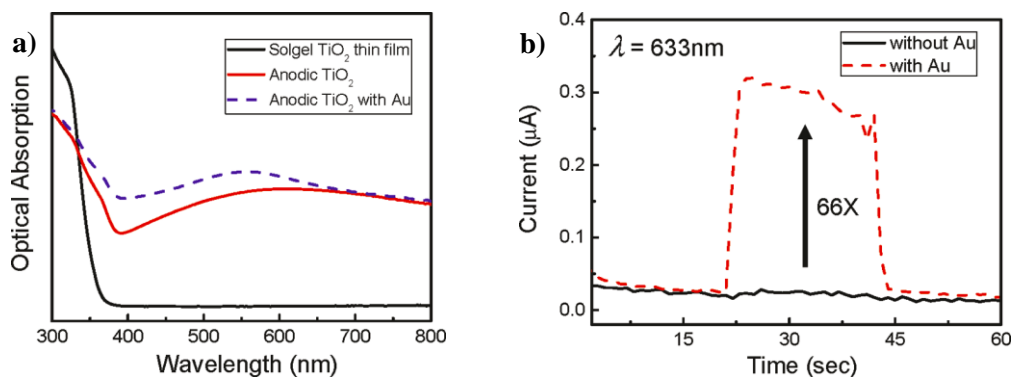
Figure 13: Absorption spectra of Anodic TiO_2 from [21] (a) and photocurrent with and without Au nanoparticles at zero bias voltage obtained by Liu group (b).

2.2.4   Hot Electron-Hole Pair Generation Model

It has been shown that that surface plasmon decay can produce electron-hole pairs in gold[24-25]. At the Au-TiO_2 interface, a Schottky junction is formed. In the case of Au nanoparticles on TiO_2, this results in a charge transfer from the TiO_2 to the gold, charging the gold negatively and the TiO_2 positively and producing a potential barrier ~0.9eV[19]. Electronic states at the metal-semiconductor interface pin the Fermi level E_F at an energy V_b below the conduction band of the semiconductor. When the metal is irradiated and a surface plasmon is induced, if the plasmon oscillation polarization wave has a phase velocity at the surface that is less than that of light in the medium with which the metal surface contacts, the plasmons are unable to decay into photons and are thus deemed non-radiative. Non-radiative plasmon decay channels include electron-electron scattering, Landau damping, and a very fast excitation of a single electron by a single photon. Initially, it was assumed that this electron excitation required that the plasmon energy exceed the work function of the metal[25]. Accordingly, high work function metals such as Ag and Au needed a sub-monolayer coating of a low work function material for any photoemission to be detected. Later, Lehman[24] showed evidence of photoemission of high work function metal particles without

coatings, which was attributed to either coherent double excitation of surface plasmons, or to sequential excitation, both of which act to excite electrons above the Schottky barrier. Briefly, spherical particle surface plasmons can be modeled as dipole oscillators in which the free electrons collectively oscillate in the harmonic potential of the positive background charge. For the dipole oscillator, the excitation (electron-hole creation) probability of a doubly–excited plasmon was found to be proportional to the square of the probability of the surface plasmon. For the sequentially excited process, this probability is multiplied by the probability that a collective excitation couples to the already excited single-particle state. Thus, photoemission is an important decay mechanism of surface plasmons. Light not redirected by the nanoparticles is absorbed, forming energetic or "hot" electron-hole pairs, which contributes to plasmon damping. The emitted photoelectrons from one electronic state are distributed over a range of final state energies due to various levels of electron cooling.

The electron-hole pairs are created by the non-radiative decay of the surface plasmon and the hot electrons can overcome the Schottky barrier or tunnel through it to become conduction electrons in the conduction band of the semiconductor, contributing to a detectable photocurrent. Knight *et. al* approximated the photoemission probability by a modified Fowler theory, which describes the number of available electrons in the system with sufficient energy to overcome (tunnel through) the potential barrier. With the Schottky barrier formed by a plasmon resonant antenna rather than a continuous film, the Fowler response is modified with a plasmon absorption spectrum factor, and the Schottky barrier height can be calculated. Details of Fowler tunneling statistical mechanics are well beyond the scope of this work, but the process should be noted as an important factor in photocurrent production. The efficiency of converting hot electrons to photocurrent is affected by the Schottky barrier height, circuit resistance, device geometries, constituent material properties, and other device-specific parameters.[15]

Correspondingly, a new model was suggested[19], shown in Figure 14. As the surface plasmon decays, the excited electrons occupy normally empty states in the metal's conduction band. Then, a significant portion of these electrons tunnel through the Schottky barrier to the TiO_2. This reduces the negative charge on the gold caused by the Schottky junction formation and begins filling the depletion region of the TiO_2. This can be probed as conductance changes in a TiO_2-Au nanoparticle film.
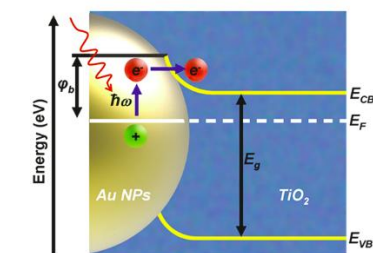
Figure 14: Plasmon-decay-induced exciton tunneling mechanism proposed by [19]

2.3   Discussion

Clearly, in the case of the charge transfer and tunneling models, plasmonic enhancement should be independent on impurity and defect levels in the TiO_2. The Liu group [21] used a sol-derived TiO_2 film relatively free of impurities as a control for their optical antenna-based model, and found that the film did not absorb or scatter any light in the visible range, and verified their near-field enhancement (concentration) model by the lack of photoresponse with or without Au nanoparticles deposited on the sol-derived film. However, although properties sol-derived films vary greatly in terms electrical and optical properties and due to sensitivity of composition, annealing environment, and deposition conditions, they should contain a high concentration of oxygen defects which serve to produce sub-band gap states. All of the films we produced had an extinction signal in the visible range. This could be attributed to Fresnel losses at the substrate

interface alone. However, other researchers have found that oxygen defects play a key role in photocurrent characteristics of TiO_2 films, as they both mediate charge transfer and produce free carriers due to stoichiometric deviations[2,8,10]. Thus, it is worth-while to further investigate sol-derived films; they should be sufficient to verify any of the three proposed mechanisms. Very few studies have employed sol-derived films to compare and analyze the proposed plasmonic enhancement mechanisms. The goal of the present work is to observe the plasmonic energy transfer effect in sol-derived TiO2-Au films, using photochemical setup as well as a multi-layered solid-state photocurrent device, and to identify which of the proposed models, if any, best describe the effect.

2.4   Experimental

Photoelectric and photoelectrochemical energy transfer in the visible region was studied in single and multilayered TiO2-Au nanoparticle film devices under irradiation at 254, 405, 532, and 650nm light at varying angles of incidence, with the goal of observing a wavelength-dependent photocurrent response. As in previous studies, evidence that any observed enhancement of photocurrent can exclusively be attributed to plasmon resonances would be the degree to which the photocurrent spectra tracks the extinction spectra of the Au nanoparticle-TiO_2 composite film. Then, photocurrent spectra comparison between devices made with relatively defect-rich sol-derived TiO_2 and with purer sputtered TiO_2 could provide evidence to the importance of the presence of sub-bandgap states and thus validate one of the models.

TiO_2 –Au samples were produced by e-beam evaporating a 5nm thick Au film onto a TiO_2 film that was produced from $Ti(OBu)_4$ precursors using the method described in section 1. After deposition of gold, the samples were annealed at 500°C for 15 minutes which causes the gold to exhibit island-like formations, effectively converting gold film into an array of

nanoparticles. For multilayered solid state devices, a new layer of TiO_2 was subsequently deposited onto the Au-TiO_2 by the spin coating of $Ti(OBu)_4$ sol, and the entire process was repeated until the desired multi-stack structure was obtained. For all samples prepared for photocurrent measurements, Indium-Tin-Oxide (ITO) coated glass microscope slides were used as substrates.

SEM images of nanoparticle arrays after annealing are shown in Figure 15. Despite the irregularity of the pattern and particle size (10-50nm), finite-difference-time-domain electromagnetic simulations of similar films carried out by Liu predicted the dominance of local "hot spot" regions between nearly touching particles, which create the intense local fields that results in dramatically increased photon absorption rates near the surface of the TiO_2.

a) b)
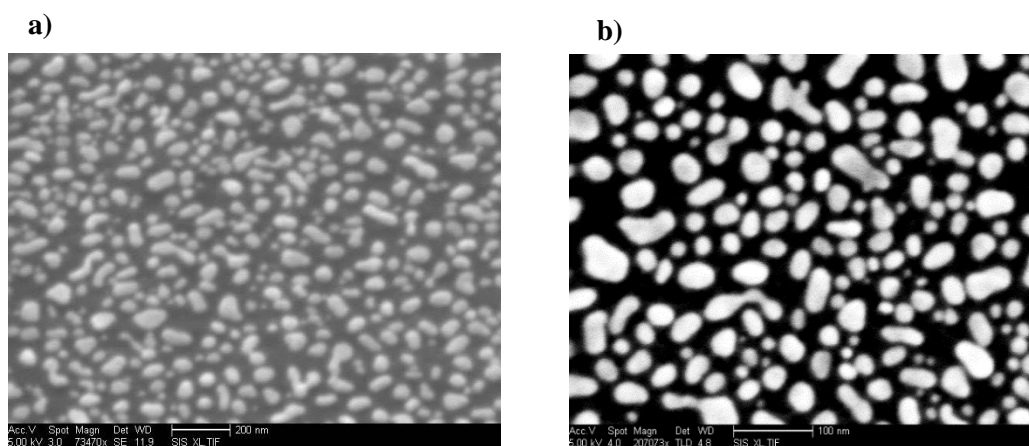
Figure 15: SEM image of 5nm thick Au island film at a), 200nm and b), 100nm length scale.

For the purposes of this work, these results enable further insight into the energy transfer mechanism, as this marks a point of contrast between the proposed models. In the light concentration model, the extent of the near-field enhancement, and thus the presence of hot spot regions, would significantly affect the observed photocurrent response. The carrier diffusion length in polycrystalline oxide materials (10-20nm) is much shorter than the absorption depth, so

in the case of surface catalysis, only photons absorbed close to the TiO_2 surface will contribute as charge recombination drastically lowers overall quantum efficiency. With light concentrated near the surface, absorption in that region would be improved leading to higher open circuit voltages and higher conversion efficiencies. By contrast, the hot-electron model proposes the creation of electron-hole pairs by the non-radiative decay of a surface plasmon, which then have increased probability of photoemission[15]. Thus, this mechanism should not depend on the presence of hot spot regions between particles. Therefore, in addition to the comparison of photoresponse between devices with varying levels of doping and defects in the TiO_2 films, a comparison between devices with and without significant presence of hot spots would be insightful. This can be accomplished by varying Au nanoparticle coverage concentrations, which dictate average inter-particle distance and thus hot spot concentration. Achieving an average inter-particle distance of 100nm should be sufficient to ensure near-field coupling is absent.

Figure 16 shows the UV-Vis extinction spectrum of TiO_2 films with and without Au nanoparticles. Also shown is the spectra for the sample after Au film deposition but before annealing. As expected, a broadband extinction signal appears due to surface coverage of the Au which leads to increased scattering. Here, the samples were deposited on bare glass microscope slides in order to further isolate absorption from Au nanoparticles. ITO-coated slides introduce another layer of Fresnel losses, and the interference patterns are more pronounced.
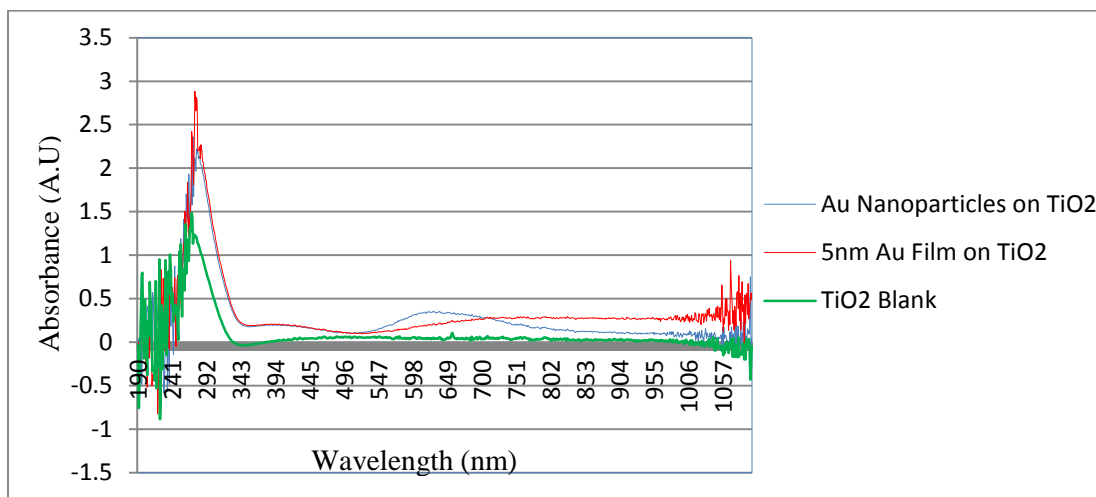
Figure 16: Absorption spectra of Au-TiO2 samples on glass substrates.

After annealing, a peak appears from 550-650 nm, which is the characteristic plasmon resonance absorption band for Au nanoparticles. The shoulder at ~390 nm is attributed to interband transitions. Below 400nm, Au absorption is dominated by interband transitions, and between 400 and 520 nm, the photon absorption spectrum contains components from both interband transitions and the plasmon resonances. At energies below this interband transition threshold, the localized surface plasmon resonance (LSPR) resonance dominates.[17] In Figure 17, an enhancement curve was obtained by normalizing the Au nanoparticle contribution with respect to the contribution from Au film before annealing treatment.
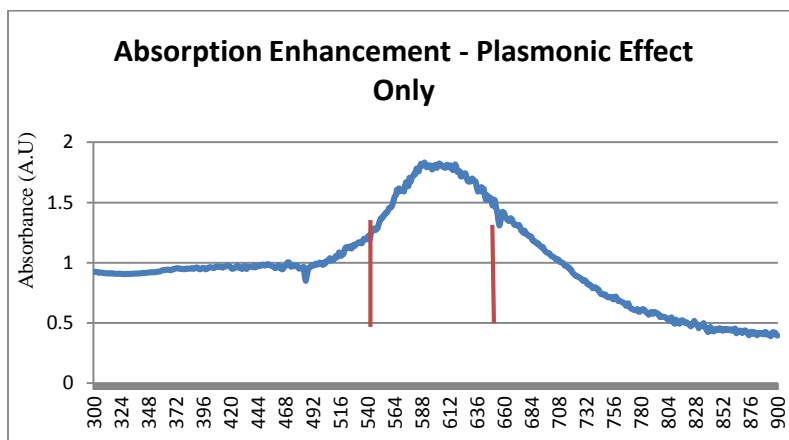
Figure 17: Absorption enhancement curve obtained by dividing the spectrum of the sample with Au NPs by the spectrum of the sample with Au film. The red markers indicate the range of typical plasmonic absorption band for Au nanoparticles.

Generally, electrical and photoelectrical characterization of TiO_2 film devices is difficult do to the polycrystalline, highly resistive nature of anatase TiO_2 films, and the difficulty in predicting the concentration of carrier recombination sites. Any such analysis must be carefully designed with carrier diffusion lengths, optical absorption depth, and interface characteristics between film and substrate and measuring electrodes understood. Employing the films as anodes in photocatalytic cells, such as 3-electrode potentiostats, is likely the ideal setup. The electrode materials and their work functions, the electrolytes, and the electrical properties of such setups are well understood, and contact resistance between the sample and the internal circuitry of the analysis computer is minimal.

Photocatalytic water splitting reaction rates of TiO_2 electrodes with Au nanoparticles in a 1M KOH solution were measured in a three-electrode photochemical cell using linear sweep voltammetry (Ideally, the cell would instead be connected to a potentiostat, and photocurrent spectra measured by irradiating with a white light source through a monochromator that provides continuously tunable monochromatic light). The reaction rates were probed by observed photocurrent enhancement. The three terminal cell contained the ITO-TiO_2-Au working

electrode, a Ag/AgCl reference electrode and a graphite counter electrode. For photocurrent response analysis, the linear sweep was run in dark conditions, with the cell irradiated by a UV diode (365nm) only, with a 3200K black body source only, and with both UV and black body radiation. The spectrum of 3200K blackbody radiation can be seen in Figure 18. Without the ability to tune wavelength, only a crude proof of concept can be expected in the photochemical cell experiment. A light chopper was also used to observe the visible light response of the sample.
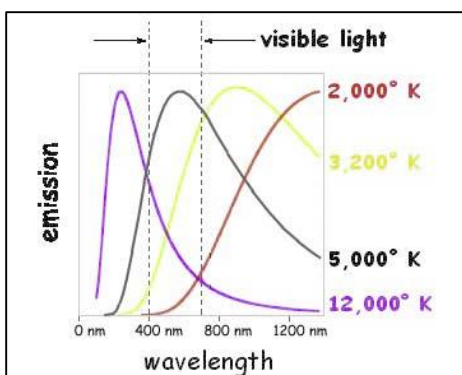
Figure 18: Blackbody Radiation diagram

The plots of the results are located in Appendix C. The results seemed to favor the presence of Au nanoparticle plasmon resonant energy transfer. The current response of the voltage sweep under visible irradiation was the highest, followed by that with UV plus visible (which is difficult to explain), UV only, and the dark run resulted in the lowest current response. Also, when a light chopper was introduced to the visible irradiation, the current response was also chopped as expected. However, the results were mostly unclear, and this investigation was tabled in favor of a solid-state device based on the device developed by Mubeen. [19]

A multi-layered solid-state device was developed by the sequential deposition of TiO_2 films by spin coating of sols and Au nanoparticles by e-beam evaporation of 5nm thick films

followed by an annealing step that produces nanoparticle arrays. ITO coated slides were used as

the conductive back electrode substrate on which the TiO_2-Au samples were deposited. A

schematic of the device is shown in Figure 19. Part (a) represents the first layer of the device and

the setup used to measure photocurrent response. Part (b) represents the final 3-stack structure,

with 3 layers of Au and 4 layers of TiO_2. After each layer was added to the device by the

sequential deposition of Au and TiO_2, absorption spectra was measured for the device. IV-t

photocurrent characterization was performed after each deposition of TiO_2 only so that top

contacts did not touch the Au directly. The photocurrent measurements were carried out during

30-60 second IV-t measurements on an Agilent B1500 semiconductor analyzer. Two tungsten

probes contact the sample through the silver contact pads, and are held at 1V bias. Within the

timeframe of the IV-t measurement, approximately single wavelength light is irradiated onto the

sample to observe photocurrent response. A 254nm 6W ultraviolet hand held lamp is used for

UV irradiation of sample. 405nm, 532nm, and 650nm lasers (5mW) were used for visible light

stimulation in the interband transition, overlap (both interband and plasmon absorption), and

plasmon resonance zones, respectively.
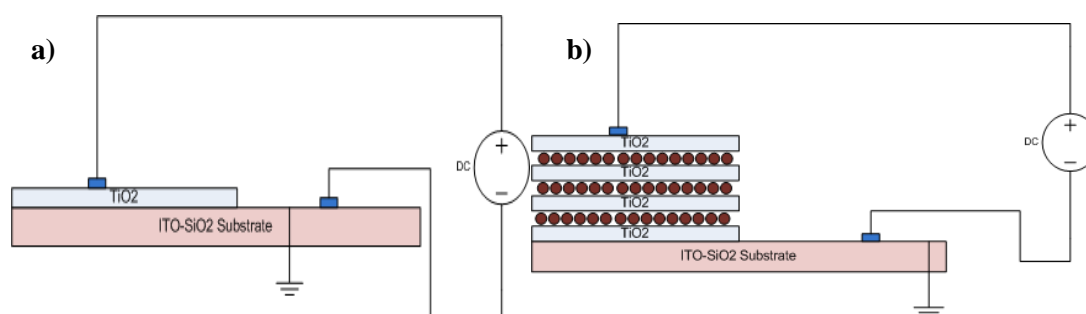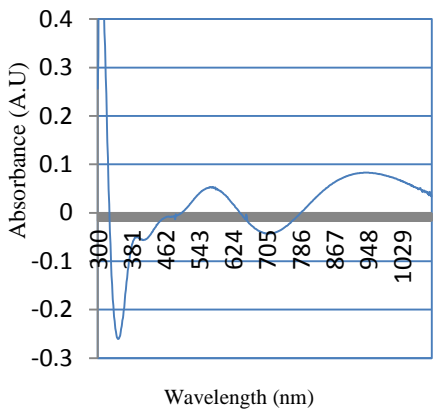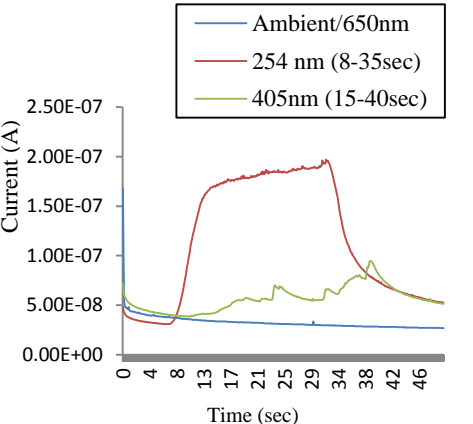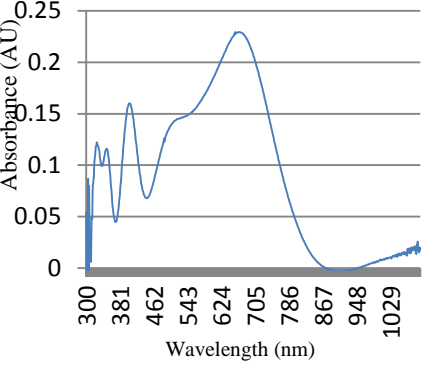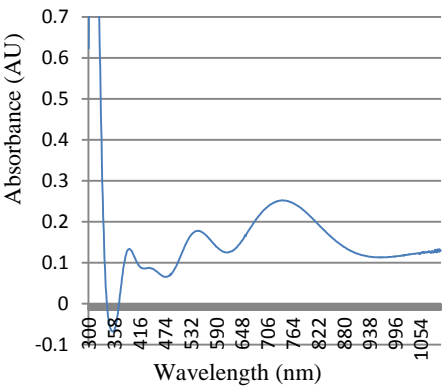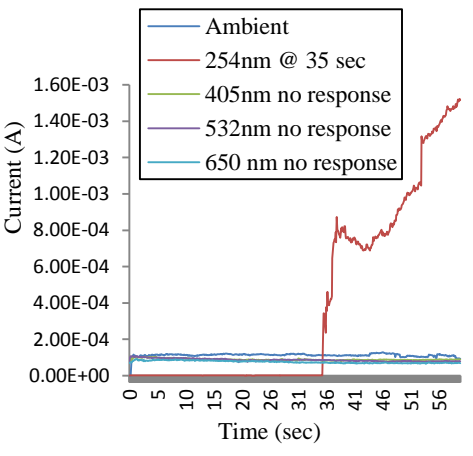
Figure 19: Initial and final device architecture for analysis of the plasmonic enhancement of photocurrent. Pads were placed on each TiO2 layer for photocurrent analysis (a). Final Device structure with alternating layers of TiO2 and Au nanoparticles (red circle) (b)

For electrical characterization, silver conductive paste was deposited on the new layer of TiO_2 as conductive contacts for the tungsten probes. Before depositing the each layer of Au, the silver contact pads were completely removed from the underlying TiO_2 surface.   In order to ensure the only contribution to measured current was that which propagated normal to the surface of the film, part of the ITO contact was masked during layer depositions. As seen in Figure 19, one probe directly contacts the ITO through the silver contact pad.
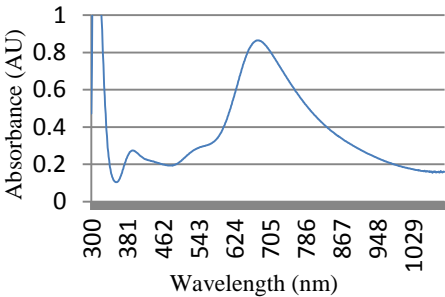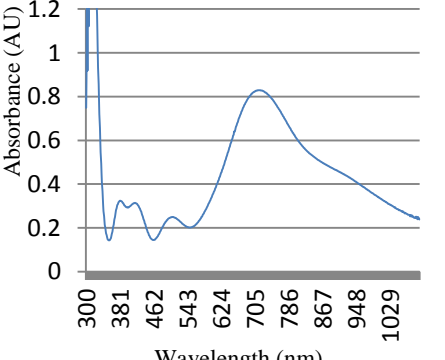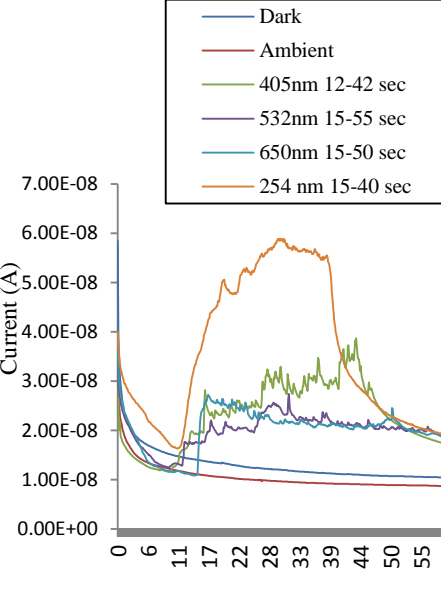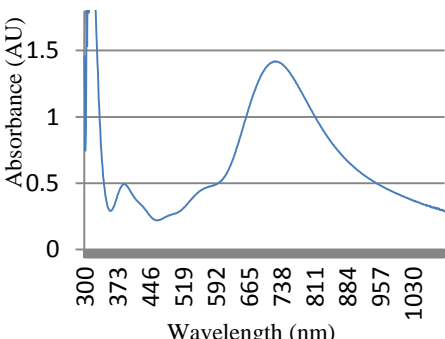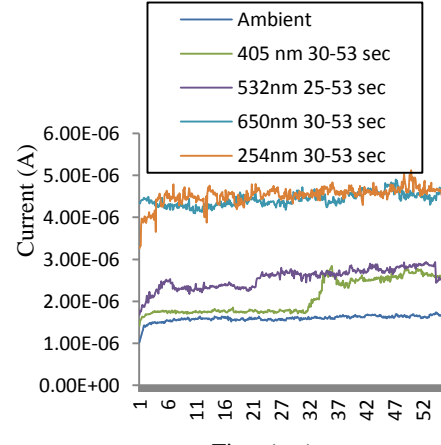
2.5   Results

Table 4 shows the absorption and photocurrent spectra measured after the addition of each layer. The photocurrent spectra includes curves for dark/ambient, and for the response to impinging light at each wavelength.

Table 4: Extinction spectra and IV-t curves for the solid state sandwich-structure device after deposition of each layer. The resulting composite structure after each deposition is denoted by the abbreviations in column 1

Layers on ITO Substrate (S): TiO$_2$(T), Au (A)	Absorption Spectra	IV-t Curve, 1V bias
T-S		
A-T-S		N/A
T-A-T-S		

Table 4: Extinction spectra and IV-t curves for the solid state sandwich-structure device after deposition of each layer. The resulting composite structure after each deposition is denoted by the abbreviations in column 1

Layers on ITO Substrate (S): TiO₂(T), Au (A)	Absorption Spectra	IV-t Curve, 1V bias
A-T-A-T-S		N/A
T-A-T-A-T-S		
T-A-T-A-T-A-T-S		

The absorption/extinction spectra for the device shows a broadband increase in the extinction due to thickness influence of absorption and the increased scattering of multiple layers. Also present is the steadily increasing LSPR peak with additional Au layers, initially centered at 650nm, indicative of ideally separated gold nanoparticles. With addition of each layer of TiO_2, which caps the Au nanoparticle layers with 70-100nm thick TiO_2, the LSPR peak is red-shifted 60-100nm. The red-shift is attributed to the increase in the dielectric constant of the medium surrounding the top gold layer relative to air; polycrystalline anatase TiO_2 dielectric constant ranges from 55-130. This effect is clearly visible in the spectra shown in Table 4. If the top-most gold layer is uncapped, the LSPR peak stayed close to 650. After capping, the resonant wavelength shifted toward 720nm. Additionally, in the case of the second and third layers of (uncapped) gold, the previous red-shifted peak of TiO_2-capped Au creates a shoulder in the absorption spectra. The broad absorption of the Au nanoparticles is a result of the inhomogeneity in size, shape, and separation of these plasmonic nanoparticles, as can be seen in the electron microscope.

With respect to the discussion of resonant energy conversion, we expect to observe increasing current under irradiation within plasmon bandwidth with each additional layer of Au nanoparticles. Under irradiation at wavelengths outside of the LSPR resonant band, we look for the absence of photoresponse which should validate the origin of photocurrent as LSPR. Beginning with the current spectrum of the single TiO_2 layer (T-S), we see a steady state current of ~35 nA under a 1 V bias voltage in dark conditions. No response was observed when 650 nm light was irradiated onto the sample, while impinging 254nm UV light resulted in a 5x increase in measured current. 254 nm (4.8eV) illumination is well above the band gap of TiO_2 and thus results in an increase in carrier concentration due to direct transitions. Interestingly, a small and relatively erratic current increase was observed under 405nm irradiation. Possible explanations

for this visible light response include the promotion of mid-gap states that exist due to impurities or oxygen vacancies, or the interaction between the electromagnetic field of the impinging laser with the tungsten probe, or other environmental factors. An absorption shoulder at 405nm cannot be distinguished in the absorption spectrum due to the presence of the Fresnel scattering between the TiO_2 and ITO layer.

A giant drop in device resistivity was observed after the deposition of Au nanoparticles and an additional TiO_2 top layer (T-A-T-S). Under the same 1V bias, dark/ambient current increased to 100µA, a 3-orders of magnitude increase from the previous single Titania layer. A nearly instant order of magnitude current increase was observed during an IV-t measurement upon impinging with 254nm UV irradiation at 35 seconds. As for the IV-t measurements for this device configuration under 405nm, 532nm, and 650nm illumination, no response was observed. These results are indeed puzzling. The increase under UV can still be explained on the basis of direct band gap transitions. Under visible irradiation, any plasmon-induced charge transfer would likely have been too small to register in the relatively large background current signal. Possible explanations for the increase in device conductivity are addressed in the discussion section below.

The next addition of Au with a TiO_2 top layer (T-A-T-A-T-S) yielded results more in line with original expectations for the device. Under dark and ambient conditions, steady-state current measured was ~10nA indicating the device resistivity had recovered to the levels of the single TiO_2 layer. A photoresponse was observed in all illuminated IV-t runs. First, a 60 second measurement with 405nm irradiation from 10 to 45 seconds yielded a steady but noisy 4x increase in current throughout the duration of the illumination, with an asymptotic decline after the light was turned off. After this measurement, a control run was conducted under ambient light; the results were identical to the initial dark run, verifying the sample had not been anomalously charged. The next 60 second IV-t run with 532nm illumination (from 15-55

seconds) resulted in a slow, steady 2x current increase throughout the duration of the illumination. Interestingly, the current did not appreciably drop after the illumination. Another control run again resulted in a steady state 10nA measured current. Then, an IV-t measurement was conducted with 650nm irradiation from 15-50 seconds. 650nm, although not at the peak resonance, is within the plasmonic absorption band for the (T-A-T-A-T-S) device, and is the only light with which we expect to observe evidence of plasmon-induced charge transfer. Upon irradiating the sample, an instant 3x current increase was observed, from 10 to 30nA, followed by a slow settling to 20nA even while still under irradiation. After one more ambient control run, an 8x current increase was observed with 254nm UV irradiation, as expected.

The IV-t measurements performed after the final Au and TiO_2 layer was added yielded more puzzling results. Again, the device resistivity was dramatically reduced, with the steady-state dark current observed between 1 and 5 μA. A small increase in current was seen upon illumination with 405nm and a smaller increase with 532nm, but none of the other wavelengths including 254nm resulted in any change in the current measured by the instrument.

2.6   Discussion

Interpreting the visible response of the two-gold-layer device (T-A-T-A-T-S) independently, we observe several interesting features. A surprising irradiation-induced current increase was seen for both 532 and 405nm light, which are both far off plasmon resonance. As discussed above, this could simply be due to direct light-matter interactions with the tungsten probes. However, for the single TiO_2 layer devoid of Au nanoparticles, no response was observed for both 532nm and 650nm illumination, so this cannot be the only influence. It is interesting to note the existence of two smaller peaks in the absorption spectrum of the device with two gold layers, which happen to be near 405 and 532nm. Although the oscillatory nature of the extinction

curve is expected due to interference effects, the presence of two separate prominent mid gap states cannot be discarded. These also could result from the irregular shapes and spacing of the nanoparticles. A nanorod aligned with incident light will display both a longitudinally oriented large resonance peak as well as a smaller transverse peak. Nanoparticle clusters also tend to exhibit multiple peaks in the absorption spectrum.[15-16] Why the response was not seen in the thicker device, even with the absorption spectra still displaying these smaller peaks, if indeed mid-gap states or additional plasmon peaks were present, is most likely due to the fact that the overall current was orders of magnitude higher than the contribution of these sub-bandgap excitations. Also worth noting is the gradually increasing nature of the measured current under 405nm and 532nm illumination. In contrast, 650nm illumination elicited an instant 3x increase and a subsequent gradual but not complete settling of the measured current. A different mechanism was likely at play for the in-resonant 650nm light.

Two possibilities are proposed to explain the response to 650nm light: first, since the metal-semiconductor interface initially charges the Au negatively and creates a Schottky barrier, the observed jump in current could be due to the discharging of the excess charge over the barrier under the 1V bias of the device. As discussed by Choi $et.$ al, [29] the ability of metal nanoparticles to accept electrons and promote interfacial charge transfer has been well studied. The accepting of electrons leads to Fermi level equilibration and a shift to more negative potentials. Thus, they argue that many of the studies that conclude that enhancement in the performance of metal-semiconductor photocatalysts and solar cells is attributed exclusively to plasmon-induced effects overlook this simple electron storage factor. Their work, like the work of the authors of the charge-transfer model, suggested Au particles accept electrons from TiO_2/dye particles. In other words, transient photocurrent decay is a result of charge trapped at the TiO_2 surface which is released upon irradiation. However, this mechanism should not depend on the impinging light

being near the plasmon resonance, so the 405 and 532nm would have showed similar instant jumps, especially since these wavelengths were both tested before the 650nm illumination.

The second proposed mechanism behind the 650nm response is explained by femtosecond relaxation dynamics of plasmons. Many such studies have been carried out on Au and Ag nanoparticle plasmons. Lehman[24] describes the decay channels of a plasmon resonance as including the very fast photoemission of electrons within the first oscillation period, Landau damping and electron-electron scattering. Beginning with an excited plasmon, the electron gas is heated, and electron-electron scattering dampens the plasmon and leads to spectral broadening of the SP absorption. A bleach signal therefore arises in the absorption spectrum, centered at the SP resonance maximum, with two positive wings at lower and higher energies. Then, as electrons cool by way of phonon collisions, the bleach signal decays after a total of 8-15ps. They also showed that incident power variation at a single wavelength resulted in a linear photocurrent response, which suggests that photocurrent is dominated by plasmonic-induced conversion of single photons to single hot electrons.

In the solid-state device devoid of an electron donor, the photocurrent might be subject to the rate-limiting factor of nanoparticle recharging from the external potential through the TiO_2. The plasmon frequency, ω_p, is directly proportional to the electron density[27], N; it can be approximated as

$$\omega_p = \left(\frac{Ne^2}{\epsilon_0 m_{eff}(1+\epsilon_m)}\right)^{1/2}.$$

Thus, if an ultra-fast creation and subsequent tunneling of electron-hole pairs within a few femtoseconds of the plasmon excitation, the nanoparticle would either accept an electron from an adjacent semiconductor crystal, or decay. Since no evidence of particle decay was observed, this discussion will focus on the former. After the initial plasmon-induced electron transfer, the

electron density will have been lowered until the nanoparticle is recharged by the adjacent TiO_2, shifting the plasmon frequency to higher wavelengths. If recharging does not happen within a few femtoseconds (time until next plasmon is excited), the results could be observed in photocurrent measurements. In the present case, the 650nm impinging light was already lower than the plasmon resonance of ~714nm (still within band), so the effect of moving further off resonance could account for the settling of current at lower levels than the original jump, assuming the system has reached a steady state and with carrier diffusion through the TiO_2 on the high-potential side of the device sufficient to recharge the particles. To date, relatively few studies on the plasmon-induced photocurrent enhancement mechanism include a discussion of the time-evolution of the mechanism, including the depletion of particles where the electron-hole pairs originated. In this light, both femtosecond relaxation and transient absorption analyses would be interesting further studies for our device.

Of course, the data from these experiments is inconclusive. The results from the single and three layer (Au) devices brought to light the possible limitations of the measurement accuracy and resolution of the instrument. The device resistivity in dark and ambient control conditions was measured to be 2-4 orders of magnitude lower compared to that measured for the device with two layers of Au nanoparticles. For the 3-layer device, a small response was observed for the 405 and 532nm light, but no photocurrent changes were measured for both 254 and 650nm light. Although this seems to validate our assumption that different mechanisms are responsible for the photocurrent enhancement at the wavelengths inside and outside of the plasmon resonance band, we cannot make this conclusion without further investigation.

Unfortunately, several attempts to reproduce the perceived photocurrent enhancement of the two-layer device proved fruitless. Two additional multi-stack devices were produced by the alternating sol deposition of TiO_2 and e-beam evaporation of Au nanoparticles. For both of these

devices, UV-Vis absorption spectra at each layer that was identical to the results of the first device, shown in Table 4. However, device resistivity registered low for each layer, similar to the single and three-layer devices in Table 4, and no photoresponse was observed for any of the visible and UV lights used to illuminate the samples.

In addition to the drastic change in overall device resistivity that cannot be explained by first principles of metal-semiconductor devices, several other factors contributed to the total experimental uncertainty. First, the device geometry was such that the path of least resistance for charge carriers is in the direction normal to the plane, so that the nanoparticles mostly likely to contribute to photocurrent enhancements are directly underneath the high potential probe. Thus, the incident laser light had to be angled in order to interact with these nanoparticles. This brings uncertainty with unfixed incident angles as well as the possibility of direct interaction with the probe. The contact pressure of the probe was not controllable for the instrument, and therefore could also account for random conductivity changes observed. The possibility of electron recombination before reaching the probe cannot be ignored. Trapped holes, surface bound hydroxyl radicals, and other surface states can act as recombination sites and cloud experimental results. The irregularity of the device with respect to nanoparticle size and spacing and the polycrystalline morphology of the underlying TiO_2 make the composite device difficult to model. The exact dielectric properties and diffusion coefficient of the TiO_2-Au composite device are therefore uncertain.

Had the observation of photocurrent enhancements proved consistent and repeatable, a set of control experiments were devised to further isolate the exact mechanism of photocurrent enhancement. First, IV-t measurement time would have been increased 10-fold to ensure a less noisy steady-state. Evidence of nanoparticle degradation would also be carefully surveyed. A device with multiple layers of TiO_2 but devoid of nanoparticles would again have been analyzed

to provide proof that photocurrent enhancement, if seen, was explicitly due to the nanoparticles. Then, a simple four-part experiment could isolate the dominant mechanism of energy transfer between the those previously proposed and even the consideration put forth in (29) – that proponents of these models might have missed the contributing factor of the release of stored charge created by Fermi-level equilibration upon metal-semiconductor contact.

In the investigation, four devices would be produced that are identical except for two variables: relative concentration of doping and defects, and nanoparticle density i.e. the density (or presence) of hot-spot regions. Then this system would be repeated with devices with thicker TiO_2 layers, which would vet the importance of a plasmon-induced increased optical path.
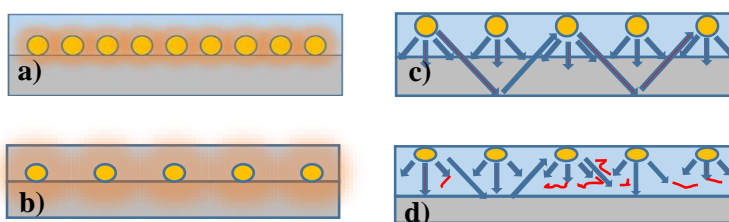
Figure 20: Device diagrams with varying hot spot concentrations (a,b) and Titania layer thicknesses (c,d)

The light concentration model relies on the presence of dopants or defects which have mid-gap energy states that can be excited by visible light, the efficiency of which can be greatly increased with plasmonic resonant field enhancements. By contrast, the direct transfer of electrons from Au to TiO_2, per the hot-electron model, would not inherently depend on donor states. Also, direct transfer is an internal process and therefore is irrespective of the presence of hot spot regions, whereas hot spot regions, according to the light concentration model, greatly increase absorption and thus affect photocurrent. The light scattering model suggests the importance of the interplay between carrier diffusion lengths and optical path lengths. According to this model, the devices with thicker TiO_2 should then see a far greater difference in response with Au particles versus without than the thinner devices, and also should depend on dopant concentrations. Therefore, the four device combinations are as follows:

Table 5: The four combinations of two key parameters to be considered in future device configurations

Device Number	Relative Defect/Doping Level	Relative Hot Spot Concentration
1	Rich	Sparse/None
2	Rich	High
3	Minimal	Sparse/None
4	Minimal	High

Thus, one device should be fabricated that corresponds to each row in Table 5. Then each device would be repeated with thicker TiO_2 layers. A relatively pure TiO_2 layer could be produced by sputtering; the concentration of hot spots could be altered by spacing the nanoparticles sufficiently as in (29). The analysis of photocurrent enhancement of the four devices described in the table would isolate the dominant mechanism by process of elimination. For example, if photocurrent enhancement occurs for both the samples with high dopant concentrations but not for the samples with minimal doping, then we expect that near-field enhancement and promotion of donor states is the dominant factor. If, on the other hand, enhancement was observed to be similar for all four devices, then the direct charge with quantum tunneling model as per the hot-electron model would best describe the mechanism. Comparison of response to irradiation near plasmon resonance and below can provide further insight to the role of the release of stored electrons. Careful observation of the change in absorption spectra with doping is essential; doping can smoothly red-shift the spectra or produce a new shoulder due to impurity levels within the band gap.

2.7 Conclusion

Photoelectric and photoelectrochemical energy transfer was studied with the purpose of pinpointing the dominant mechanism of energy transfer that has been observed in several studies as photocurrent enhancement under visible radiation in photochemical and solar cells. For both a photochemical cell setup, in which photoanodes were fabricated by depositing Au nanoparticles on TiO_2 and linear sweep voltammetry was used for photoresponse analysis, and the solid-state setup, in which Au nanoparticles were embedded in TiO_2, results were inconclusive. For the latter case, however, some evidence of a plasmonic enhancement was observed. The nature of the response seen lead to the development of a set of control experiments that could provide valuable insight into the performance-boosting characteristics of plasmonic nanoparticles. Based on the observations here and throughout literature, the mechanism of energy transfer most likely includes both direct charge transfer by way of quantum tunneling as well as near-field enhancement that effectively traps light inside absorbing layers to increase power conversion efficiency. Future investigations should include a systematic analysis of photoresponses of devices with varying doping/defect levels and hot spot concentrations as described in Table 5. Additionally, unknown variables and experimental uncertainty needs to be minimized; it is proposed that a more reliable experimental setup be used. The photoelectrochemical cells abound throughout literature provide a clear picture of plasmonic nanoparticle influence on the photocatalytic activity of semiconductor anodes, with all experiment parameters well understood. This is the type of cell used in this study, but instead of crude linear sweep voltammetry, the cell should be connected to a high-quality three-terminal potentiostat (Figure 21).
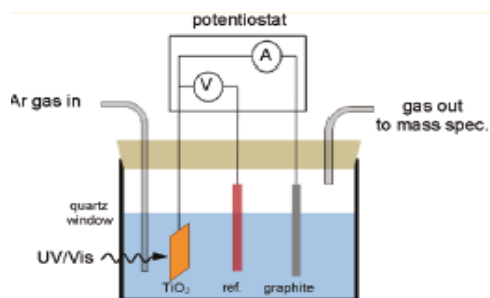
Figure 21: Three Terminal Potentiostat connected to photochemical cell.

The blackbody emitter used in the present study should be replaced with a white light source with a continuously tunable monochromator to enable true wavelength-dependent photocurrent response analysis. Later modifications to the device might include Au nanoparticle shape and spacing tailoring to maximize achievable plasmon-induced enhancements.

Appendix A

Quantum Dot Sensitization

The large-scale use of photovoltaic devices for electricity generation remains costly in comparison to conventional methods. First generation solar cells do not harvest any of the visible side of the solar spectrum, and are limited by the Shockley-Queisser efficiency limit of 32% energy conversion. To achieve the goals of efficient clean energy, a new generations of solar cells must emerge, capable of harvesting incident photons with greater efficiency. Semiconductor nanocrystals, or quantum dots, have become a hot topic for light energy conversion. They can be utilized in solar cells to make metal-semiconductor Schottky junction cells, polymer-semiconductor hybrid solar cells, and quantum dot-sensitized solar cells. Quantum Dot (QD) Sensitized Solar Cells work analogously to Dye-Sensitized Solar cells (DSSC) with a couple distinct advantages: The bandgap/absorption is easily adjustable by the size of the particles, the band edge type of absorption behavior is most favorable for effective light harvesting, and the surface properties of the particles can be modified in order to increase the photostability of the electrodes. Quantum dot band energies can be modified through size control, which offers the possibility of controlling photoresponse of the cell. Most importantly, QD based solar cells can potentially transcend Shockley-Queisser limits. If QD based solar cell energy conversion can be demonstrated, and can be produced in economically viable ways, solar energy could become the centerpiece of new energy production.

Here we attempted to create QD sensitized solar cells by evaporating and spin coating quantum dots onto TiO_2 thin films. Once verified through UV-Vis characterization and imaging excitation, a systematic study of the optical and electrical properties of ordered and

self-assembled quantum dots on thin films would be undertaken and compared to the baseline device with QDs spun or evaporated (disordered).

Two simple methods were attempted to incorporate CdSe quantum dots into or on top of TiO_2 films. First, the CdSe dots, which were dissolved in Toluene, were spin-coated onto TiO_2 films. This was attempted with annealed TIO_2 films as well as TiO_2 sols that had just been spun. The second method involved the drop-wise addition of CdSe-Toluene in varying amounts, from 2 drops to 100μl, into the TiO_2 sol prior to deposition.

Several attempts were made to fabricate CdSe-sensitized TiO_2 samples on glass slides. A comparison of the UV-Vis absorption spectra of the bare CdSe quantum dots, the bare TiO_2 film, and the composite film would clearly verify whether the CdSe quantum dots were deposited in sufficient concentrations. However, none of the samples produced displayed and increased extinction compared to the bare TiO_2. This work was abandoned in favor of the metal nanoparticle plasmonic work, as much more practical deposition methods were available.

Appendix B

Printable Photonics

The ability to fabricate structures from the micro and nanoscale with high precision is of crucial importance to the advancement of micro- and nanotechnology. Nanoimprint Lithography (NIL) is a lithographic technique for high-throughput patterning of polymer nanostructures at high precision and low cost. NIL is a direct mechanical deformation of a resist material and has achieved remarkable resolution of features. The resist is patterned by a hard mold which is pressed into the softer resist. Thus, the requirements of a resist are as follows: First, it must be easily deformable under pressure and have good mold releasing properties. The latter is especially important when considering scaling effects; high surface area contact of the mold leads to high adhesion forces. Second, it must have good mechanical strength to maintain pattern integrity yet sufficiently low viscosity so print can be done in practical time (the squeezed material needs to be swept away). We propose that a deposited sol-gel film, before annealing, meets all of these requirements. If a pattern could be imprinted into a spin-coated TiO_2 sol film, and it maintains integrity without cracking during the annealing process, then the process could be of great benefit to researchers requiring high-fidelity patterned Titania nanostructures at low cost.

A proof of concept investigation was carried out using tens-of-microns thick blades to stamp multiple parallel channels in a Titania thin film using a lab-made stamp machine. Though the films seemed to hold their integrity after the pattern was printed and the film was annealed and transformed to anatase crystalline form, the edges of the patterns seemed to suffer embrittlement and cracking. Improvement of annealing strategy could solve these issues.

Appendix C

Figures
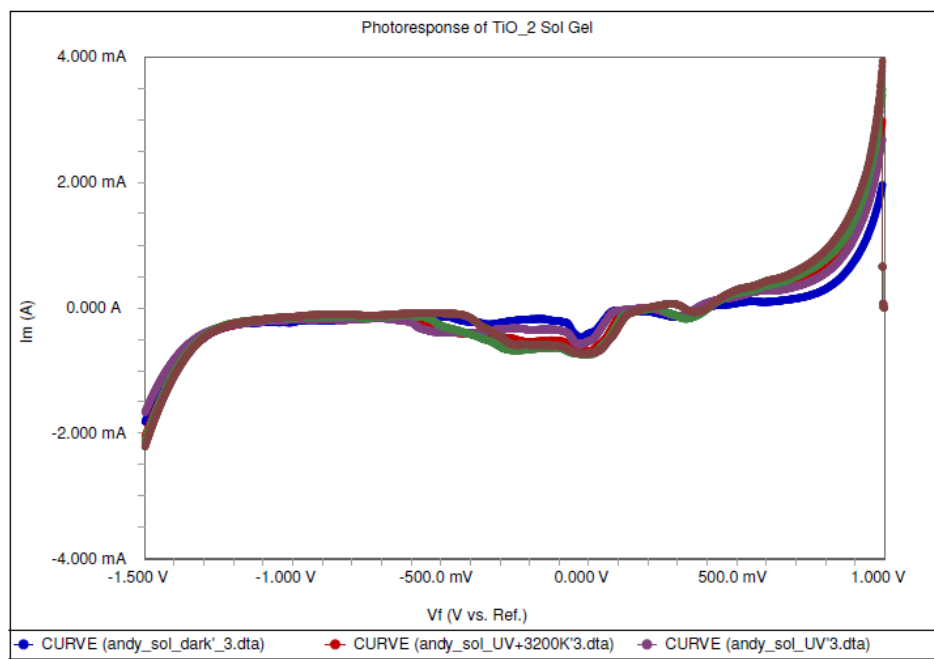
Figure 22: Linear Sweep Voltammetry results. The blue line represents the IV sweep with no light. Both UV (purple) and visible (brown, green) irradiation resulted in a current enhancement. The red line represents a sweep under UV+Vis radiation.
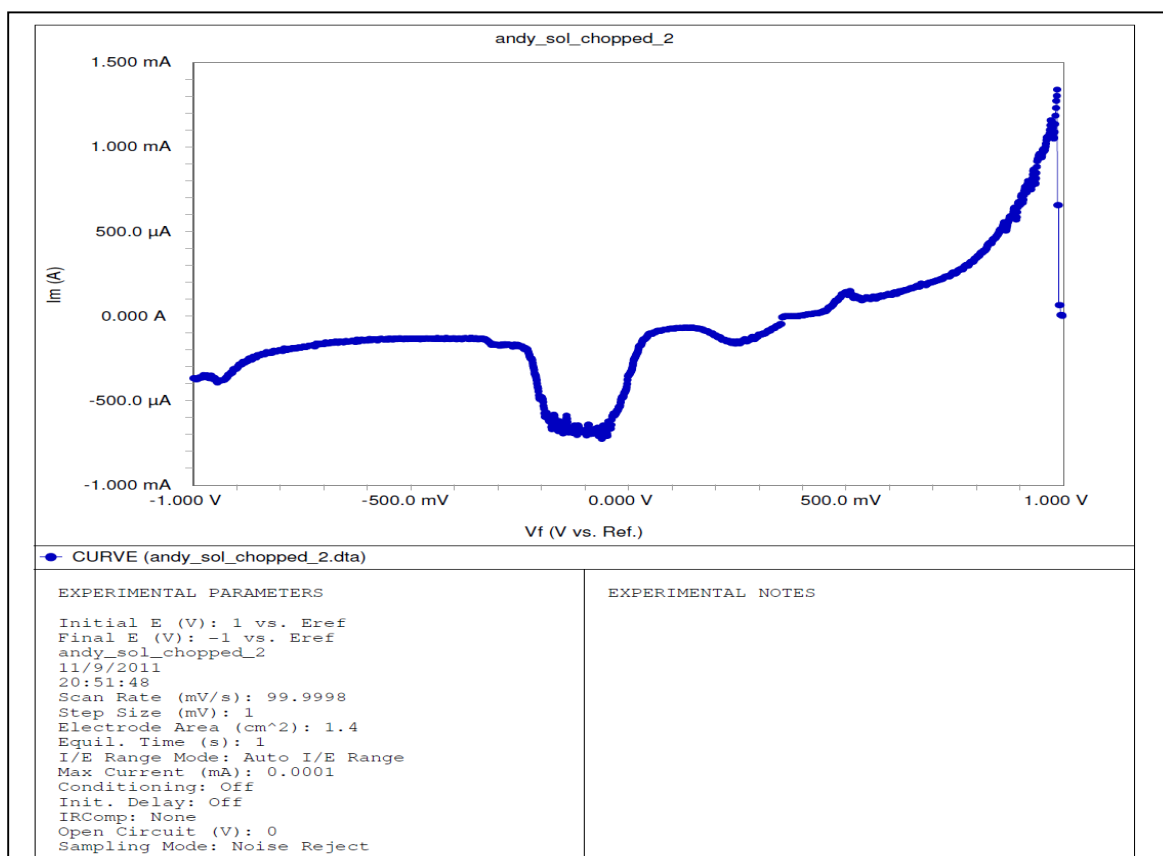
Figure 23: IV Sweep under chopped visible light. Faint choppiness in the signal only provides crude evidence that the visible light influences current.
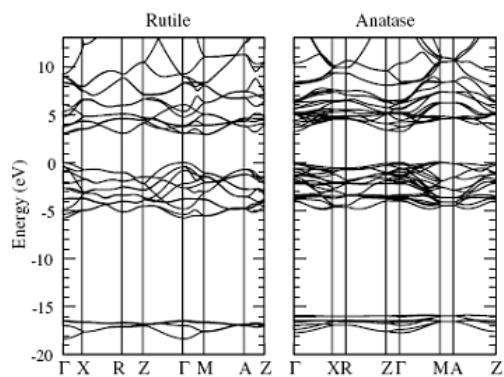
Figure 24: Band Diagram of Rutile and anatase TiO_2

References

1. C.J. Brinker, G.W. Scerer, "Sol-Gel Science" (Academic Press, San Diego, 1990).

2. Y. Hamasaki, S. Ohkubo, K. Murakami, H. Sei, G. Nogami. Photoelectrochemical Properties of Anatase and Rutile Films Prepared by the Sol-Gel Method, *J. Electrochem. Soc.* **1994**, 141, 660-663.

3. M. Bedu, G. Sagarzazu, T. Gacoin, P. Audebert, C. Weisbuch, L. Martinelli. Sol-gel planar waveguides for improved fluorescence microarrays. *Thin Solid Films.* **2010**, 518, 4450-4457.

4. I. Senain, N. Nayan, H. Saim. Structural and Electrical Properties if TiO_2 Thin Film Derived from Sol-gel Method using Titanium (IV) Butoxide, **2010**, 2.

5. A.K. Ray, S. Tracey, B. McQuillin, S. Hodgson. Optical studies on sol-gel derived titanium dioxide films. *IEE Proc. –Sci. Meas. Technol.,* **2000**, 147, 301-305.

6. Z. Wang, U. Helmersson, P-O Kall. Optical Properties of anatase TiO_2 thin films prepared by aqueous sol-gel process at low temperature. *Thin Solid Films.* **2002**, 405, 50-54.

7. J.C. Manifacier, J. Gasiot, J.P FIllard. A simple method for the determination of the optical constants n, k, and the thickness of a weakly absorbing film. *J. Phys. E: Sci. Instrum.* **1976**, 1, 1002.

8. Q. Fan, B. McQuillin, A.K. Ray, M.L. Turner, A.B. Seddon. High density, non-porous anatase titania thin films for device applications. *J. Phys D: Appl. Phys.* **2000**, 33, 2683-2686.

9. K. Kamiya, K. Tanimoto, T. Yoko. Preparation of TiO_2 fibres by hydrolysis and polycondensation of $Ti(O-i-C_3H_7)_4$. *J. Mater. Sci. Let.* **1986** 5, 402-404.

10. M. Sellers, E. Seebauer. Manipulation of polycrystalline TiO_2 carrier concentration via electrically active native defects. *J. Vac. Sci. Tehnol. A.* **2011**, 29, 6.

11. D.J. Kim, S.H. Hahn, S.H. Oh, E.J. Kim, Influence of calcination temperature on structural and optical properties of TiO_2 thin films prepared by sol-gel dip coating. *Materials Letters.* **2002**, 57, 355-360.

12. P. Ji, M. Takeuchi, T-M. Cuong, J. Zhang, M. Matsuoka, M. Anpo. Recent Advances in visible light-responsive titanium oxide-based photocatalysts. *Res. Chem. Intermed.* **2010**, 36, 327-347.

13. P. Belleville, Functional coatings; The sol-gel approach. *C.R. Chimie.* **2010**, 13, 97-105.

14. R. Swanepoel. Determining refractive index and thickness of thin flms from wavelength measurements only. *J. Opt. Soc. Am. A.* **1985**, 8, 1339-1343.

15. M. Knight, H. Sobhani, P. Nordlander, N. Halas. Photodetection with Active Optical Antennas. *Science.* **2011** 332, 702-704.

16. N. Halas, S. Lal, W-S Chang, S. Link, P. Nordlander. Plasmons in Strongly Coupled Metallic Nanostructures. *Chem. Rev*. **2011**, 111, 3913-3961.

17. E. Thimsen, F. Le Formal, M. Gratzel, S. Warren. Influence of Plasmonic Au Nanoparticles in the Photoactivity of Fe_2O_3 Electrodes for Water Splitting. *Nano. Lett.* **2011**. 11, 35-43.

18. W.H. Leng, P.R.F. Barnes, M. Juozapavicius, B. O'Regan, J.Durrant. Electron Diffusion Length in Mesoporous Nanocrystalline TiO_2 Photoelectrodes during Water Oxidation. *J. Phys. Chem. Lett.* **2010**, 1, 967-972 .

19. S. Mubeen, G. Hernandez-Sosa, D. Moses, J. Lee, M. Moskovits. Plasmonic Photosensitization of Wide Gap Semiconductor: Converting Plasmons to Charge Carriers. *Nano Lett.* **2011**, 11, 5548-5552.

20. I. Thomann, B. Pinaud, Z. Chen, B. Clemens, T. Jaramillo, M. Brongersma. Plasmon Enhanced Solar-to-Fuel Energy Conversion. *Nano Lett.* **2011**,11, 3440-3446.

21. Z. Liu, W. Hou, P. Pavaskar, M. Aykol, S. Cronin. Plasmon Resonant Enhancement of Photocatalytic Water Splitting Under Visible Illumination. *Nano Lett.* **2011**,11, 1111-1116.

22. Y. Tian, T. Tatsuma. Mechanisms and Applications of Plasmon-Induced Charge Separation at TiO_2 Films Loaded with Gold Nanoparticles. *J. Am. Chem. Soc.* **2005**, 127, 7632-7637.

23. R. Pala, J. White, E. Barnard, J. Liu, M. Brongersma. Design of Plasmonic Thin-Film Solar Cells with Broadband Absorption Enhancements. *Adv. Mater.* **2009**, 21, 3504-3509.

24. J. Lehmann, M. Mershdorf, W. Pfeiffer, A. Thon, S. Voll, G. Gerber. Surface Plasmon Dynamics in Silver Nanoparticles Studied by Femtosecond Time-Resolved Photoemission. *Phys. Rev. Lett.* **2000**, 85, 2921-2923.

25. J. Hofman, W. Steinmann. Plasma Resonance in the Photoemission of Silver. *Phys. Stat. Sol.* **1969**, 30, 53-55.

26. J. Yu, G. Dai, B. Huang. Fabrication and Characterization of Visible-Light-Driven Plasmonic Photocatalyst Ag/AgCl/ TiO_2 Nanotube Arrays. *J. Phys. Chem. C.* **2009**, 113, 16396-16401.

27. S. Link, M. El-Sayed. Spectral Properties and Relaxation Dynamics of Surface Plasmon Electronic Oscillations in Gold and Silver Nanodots and Nanorods. *J. Phys. Chem. B.* **1999**, 103, 8410-8426.

28. H. Atwater, A. Polman. Plasmonics for improved photovoltaic devices. *Nature Materials*. **2010**, 9, 205-213.

29. H. Choi, W.T. Chen, P. Kamat. *Know Thy Nano Neighbor.* Plasmonic *versus* Charging Effects of Metal Nanoparticles in Dye-Sensitized Solar Cells. *ACS Nano.* **2012**, 134, 7109-7116.

30. P. Kamat. Quantum Dot Solar Cells. Semiconductor Nanocrystals as Light Harvesters. *J. Phys. Chem.* **2008**, 112, 18738-18754.

31. R. Vogel, P. Hoyer, H. Weller. Quantum-Sized PbS, CdS, AgzS, Sb&, and Bi& Particles as Sensitizers for Various Nanoporous Wide- Bandgap Semiconductors. *J Phys. Chem.* **1994**, 98, 3183-3188.

32. N. Treat, L. Campos, M. Dimitriou, B. Ma, M. Chabinyc, C. Hawker. Nanostructured Hybrid Solar Cells: Dependence of the Open Circuit Voltage on the Interfacial Composition. *Adv. Mater.* **2010**, 22, 4982-4986.

33. L. Campos, I. Meinel, R. Guino, M. Schierhorn, N. Gupta, G. Stucky, C.J. Hawker. Highly Versatile and Robust Materials for Soft Imprint Lithography Based on Thiol-ene Click Chemistry. *Adv. Mater.* **2008**, 20, 3728-3733.